

Article

Compressive Behavior of a Fully Prefabricated Lifiable Connection for Modular Steel Construction

En-Feng Deng ¹, Jun-Yi Lian ¹, Zhe Liu ^{2,3,*}, Guang-Cao Zhang ¹, Shi-Bo Wang ⁴ and Dian-Bin Cao ⁵

¹ School of Civil Engineering, Zhengzhou University, Zhengzhou 450001, China; dengenfeng@zzu.edu.cn (E.-F.D.); lianjunyi@gs.zzu.edu.cn (J.-Y.L.); zgczgp@163.com (G.-C.Z.)

² School of Civil Engineering, Shandong Jianzhu University, Jinan 250101, China

³ Shandong Winbond Construction Group Co., Ltd., Weifang 262500, China

⁴ Zhengzhou Urban Construction Group Investment Co., Ltd., Zhengzhou 450001, China; shibo131210@163.com

⁵ Jinan Rail Transit Group Co., Ltd., Jinan 250101, China; zsgq2022@126.com

* Correspondence: liuzhe0624@126.com

Abstract: Modular steel construction (MSC) consists of the off-site prefabrication of a fully finished module and the on-site assembling of the module unit. The popularity of MSC is on the rise, attributable to its technical advantages of speed and quality of buildings with repetitive units. Inter-module connection is critical for the overall stability and load-bearing capacity of MSC. An innovative, fully prefabricated liftable connection (FPLC) using standard corner fittings and long stay bolts is proposed in this paper. This paper focuses on the axial compressive behavior and design of FPLC. Five full-scale specimens were tested under axial compression. Local buckling of the column and shear of the long stay bolts were observed during the test. It can be concluded from the test results that the load-bearing capacity may decrease as the number and diameter of the stay bolts increase. A three-dimensional nonlinear finite element model (FEM) was developed and validated against the test results by general purpose finite element software ABAQUS. Furthermore, a parametric study was conducted using the verified FEM to provide a better understanding of the axial compressive behavior of the FPLC. The results of the parametric study indicated that the corner fitting can be up to 15% lighter for columns with thicknesses of 6 mm and 8 mm without substantial reduction of the axial load-bearing capacity of the FPLC. Moreover, the location of the column can be adjusted to achieve a uniform Von Mises stress and equivalent plastic strain (PEEQ) distribution of the connection. The presented research work provides an engineering-practical inter-module connection on its axial compressive behavior, which will provide helpful references for further application of MSC.

Keywords: modular steel construction; corner fitting connection; monotonic axial load test; parametric analysis; design improvement



Citation: Deng, E.-F.; Lian, J.-Y.; Liu, Z.; Zhang, G.-C.; Wang, S.-B.; Cao, D.-B. Compressive Behavior of a Fully Prefabricated Lifiable Connection for Modular Steel Construction. *Buildings* **2022**, *12*, 649. <https://doi.org/10.3390/buildings12050649>

Academic Editor: Paulo Santos

Received: 24 April 2022

Accepted: 11 May 2022

Published: 13 May 2022

Publisher's Note: MDPI stays neutral with regard to jurisdictional claims in published maps and institutional affiliations.



Copyright: © 2022 by the authors. Licensee MDPI, Basel, Switzerland. This article is an open access article distributed under the terms and conditions of the Creative Commons Attribution (CC BY) license (<https://creativecommons.org/licenses/by/4.0/>).

1. Introduction

As a new style of construction form, modular steel construction (MSC) has attracted more and more attention from scholars and engineers around the world in recent years. In contrast to traditional on-site construction, MSC is a kind of highly integrated prefabricated building with various exceptional advantages. Generally, the volumetric modules and decorations in the units are manufactured in off-site factories and transported to the construction site [1]. Then, laborers assemble the prefabricated module units and complete the connection of the module units on-site. In this way, the construction with full building function can be put into use as soon as possible. It brings higher construction speed, lower construction costs, greener construction for human beings, and less pollution for society [2–4]. Currently, MSC has been widely used in structural-similar buildings, especially hotels, schools, apartments, and offices in some European countries [5,6]. The Chinese built a post-disaster hospital named Huoshenshan Hospital in only 10 days to

handle the explosive growth of patients because of COVID-19 using MSC, as shown in Figure 1a [7]. The world's tallest prefabricated skyscrapers will rise in Singapore and almost 3000 vertically stacked modules are being made in Malaysia. The three-dimensional visualization is shown in Figure 1b [8].



Figure 1. Mid-to-high modular construction: (a) Huoshenshan Hospital [7]; (b) 19 m tall towers [8].

The structural system is critical to guarantee the structural stability and safety of MSC. Lawson and Ogden [9,10] introduced various connections for light steel modular construction. Kim et al. [11] verified the applicability and feasibility of MSC. Later, several structural systems were proposed. Park et al. [12] and Andrade et al. [13] verified the applicability of the “modular in-fill construction method” where modules can be recessed in the primary frame. Hou et al. [14,15] verified that precast exterior wall panels with steel tee energy absorbers can provide more stable behavior in comparison with conventional exterior walls. A new material model was developed and the reported low-rise moment-resisting frames were employed and redesigned. It provided a brand-new design idea to achieve different structural and nonstructural performance objectives in the steel moment-resisting frame.

The success of a high-performance connection system can ensure efficient load transfer systems [16]. Therefore, the performance of the connection, including the ability to load-resist, the load-transferring mechanism, and assembling convenience, has attracted extensive interest from scholars in recent years. Various researchers are devoted to studying the behavior of the connections using experimental methods, numerical simulations, and theoretical analyses. Annan et al. [17] provided a semi-rigid welded stringer-to-beam connection in a typical modular construction, as shown in Figure 2a. The seismic performance of a welded frame was investigated by experimental research. Deng et al. [18] proposed a bolted connection with a welded cover plate for square hollow section columns, as shown in Figure 2b, and conducted seven full-scale T-shape connection tests under monotonic and cyclic load.

However, these connections are inadequate in middle columns because of the lack of operating space. Chen et al. [19] offered an innovative rotary inter-module connection for modular steel buildings, as shown in Figure 2c. The mechanical performance of the connection was studied through two tensile and two shear resistance tests. Dai et al. [20] introduced a novel plug-in self-lock joint for modular steel construction, as shown in Figure 2d, and the seismic performance of the plug-in self-lock joints was studied by analyzing the results of eight full-scale experiments. Sanches et al. [21] proposed a new vertical post-tensioned connection for MSC, which was comprised of a post-tensioned threaded rod installed inside hollow structural section columns and a steel box placed between two modules, as shown in Figure 2e. Dhanapal et al. [22,23] introduced a state-of-the-art VectorBloc connection that used state-of-the-art cast-steel connectors and hollow structural members, as shown in Figure 2f. Six full-scale specimens were built and tested under

axial compression and axial tension. Hou et al. [24] presented a bolted base connection and investigated the seismic performance of the connection experimentally. Furthermore, the response of the connection under combined axial compression and weak-axis lateral load was reported [25]. Chen et al. [26] investigated the seismic performance of an innovative self-locking inter-module connection experimentally, numerically, and theoretically. Zhai et al. [27] introduced a bolted-cover plate corner connection, and the monotonic and cyclic loading on five specimens were carried out to investigate the seismic performance of the connection. Deng et al. [28] summarized the state-of-the-art inter-module connections. Most of the inter-module connections use bolt-fastened seal plates [29,30], internal plates [31], ceiling beams, and floor beams [32,33]. Zhang et al. [34] introduced the seismic performance of the column-to-corner fitting connection in MSC. However, these previous connections mentioned above have limitations for practical operation in terms of the difficulty of assembling on-site and lifting the module unit.

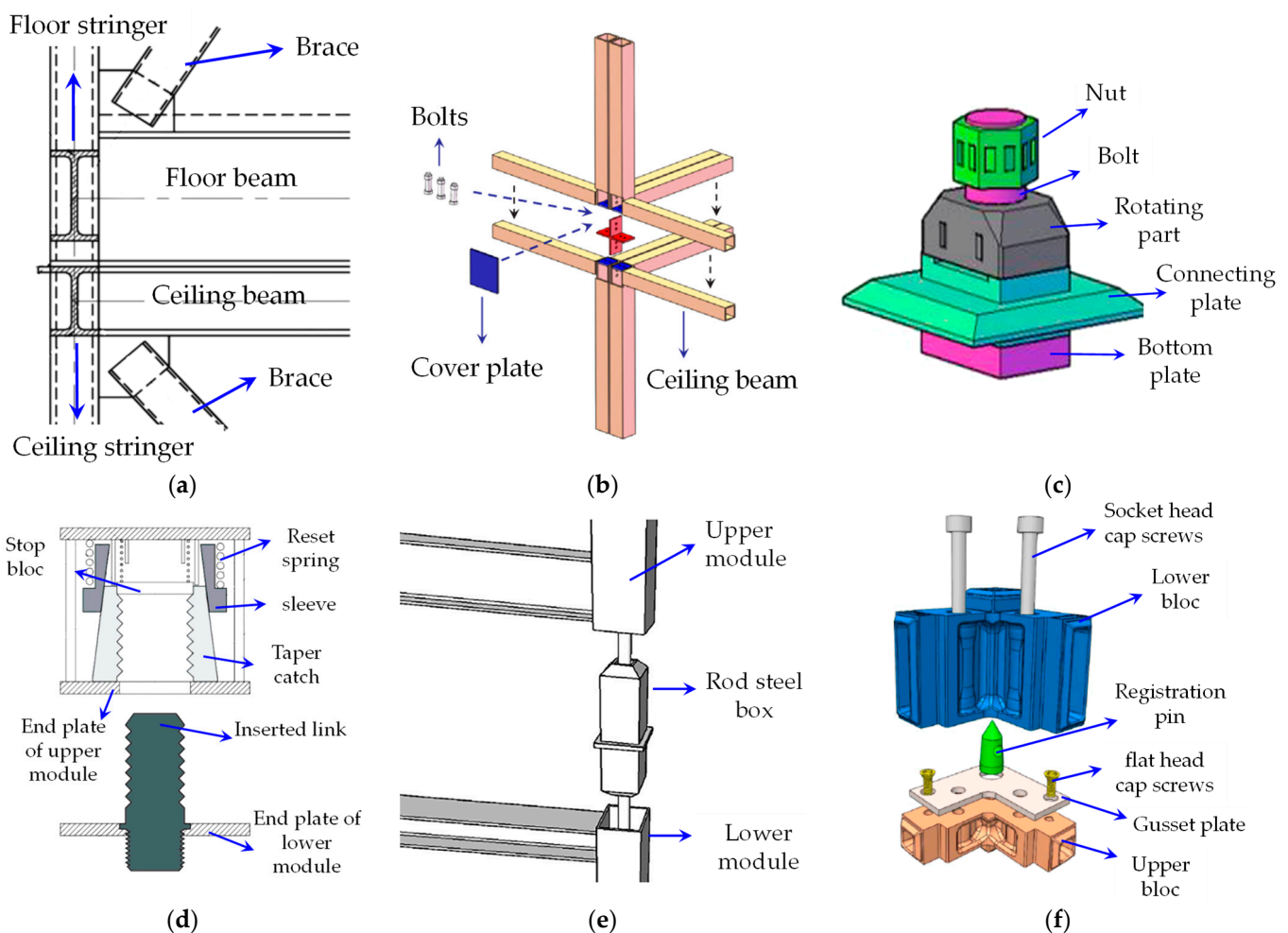


Figure 2. Representative inter-module connections for MSC: (a) welded connection [17]; (b) bolted connection [18]; (c) rotary connection [19]; (d) plug-in self-lock connection [20]; (e) vertical post-tensioned connection [21]; and (f) VectorBloc connection [22,23].

In this paper, a novel fully prefabricated liftable connection (FPLC) for MSC is proposed. The performance of the FPLC, subjected to axial compression load, was studied experimentally and numerically. Five full-scale specimens that considered various parameters were tested under axial compression. Then, numerical simulation based on the tests was conducted. The boundary condition and interactions of the model were established using commercial finite element analysis (FEA) software ABAQUS. Moreover, parametric analysis was conducted through 53 FEA models. The effect of the crucial factors that influ-

enced the axial load-bearing capacity of the FPLC was revealed. The design improvements for the FPLC were consequently proposed, which would provide useful guidance for the design of MSC.

2. Conceiving of the Fully Prefabricated Lifiable Connection

Figure 3 shows the configuration of the innovative connection and the assembling process. The FPLC includes upper and lower columns with hollow square structural (HSS) sections, standard container corner fittings, and a T-shaped gusset plate with reserved bolt holes and long stay bolts, as shown in Figure 3. The columns are welded vertically on the corner fittings by butt weld. When the lower modules are installed on site, a gusset plate is attached to the upper corner fitting using a bolt connector, as shown in Figure 3. The vertically stacked corner fittings are connected with specially made bolt clamps. The bolt connector has an internal plate, and the bolts vertically fasten the internal plates of the upper and lower corner fitting together. After that, the upper modules are hoisted through the corner fitting to the gusset plate. The locating hole has been prefabricated on the horizontal gusset plate. During installation, one end of the bolt sleeve was put on the bolt nut through the operating hole and another end was rotated to drive the nut to rotate and fasten the connection, as shown in Figure 4. Generally, steel-plate shear walls, braces, and other lateral-force resisting systems can be combined with this connection to enhance the lateral resistance of the mid- to high-rise MSC.

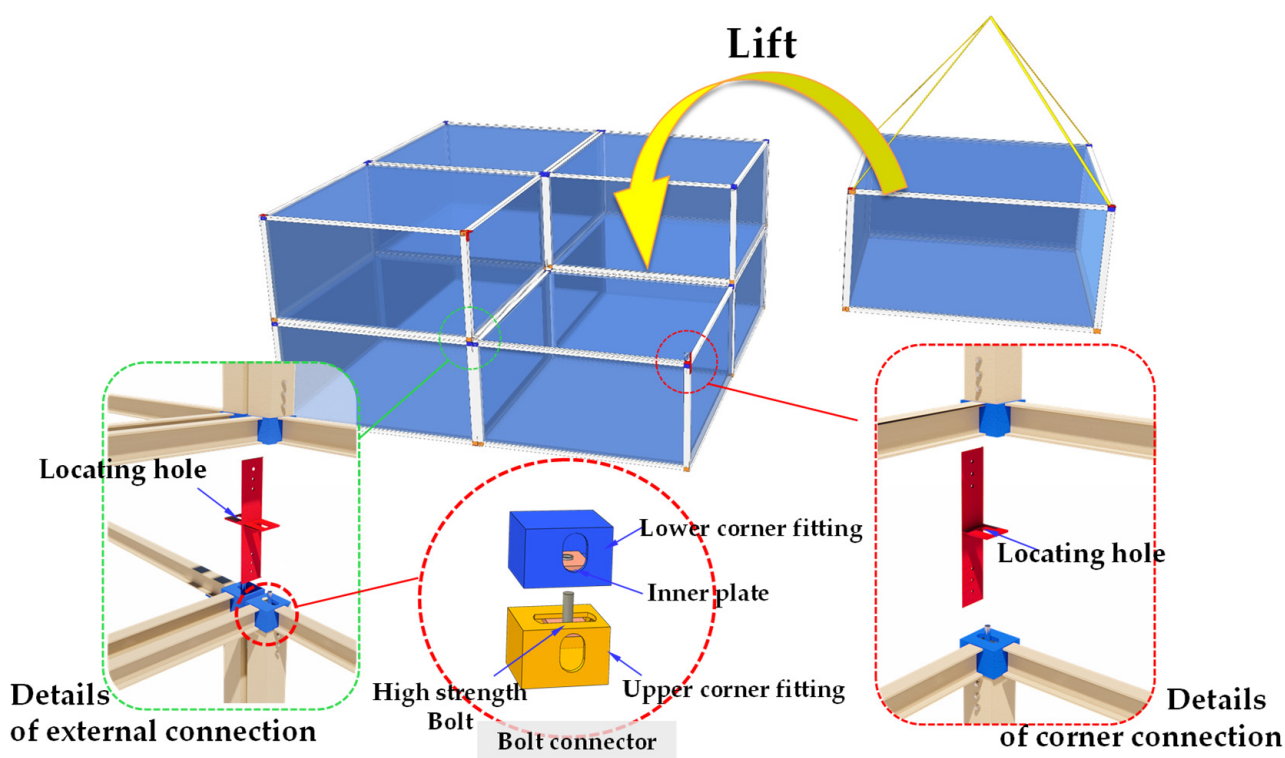


Figure 3. Details of the innovative connection.

Compared to the previous connections, the PFLC has great potential to be applied in MSC with some prominent advantages. The characteristics of this connection can be described in three aspects. (a) Easy to be hoisted: it is easy to lift the module unit by the corner fitting and this can decrease construction time effectively. Meanwhile, the corner fitting and the locating hole in the horizontal gusset plate are preferred for locating the module unit accurately. (b) Easy to be disassembled: the FPLC permits no on-site welding between adjacent modules to realize a fully prefabricated joint. When the building needs to be dismantled and reconstructed in a different place, the module unit can be disassembled by the long stay bolts and bolt connectors quickly, which is favorable for recycling demands.

(c) Excellent mechanical property: the long stay bolts can fasten vertical module units and transfer vertical forces. The bolt connector can tie the corner fitting and the gusset plate together to resist vertical separation.

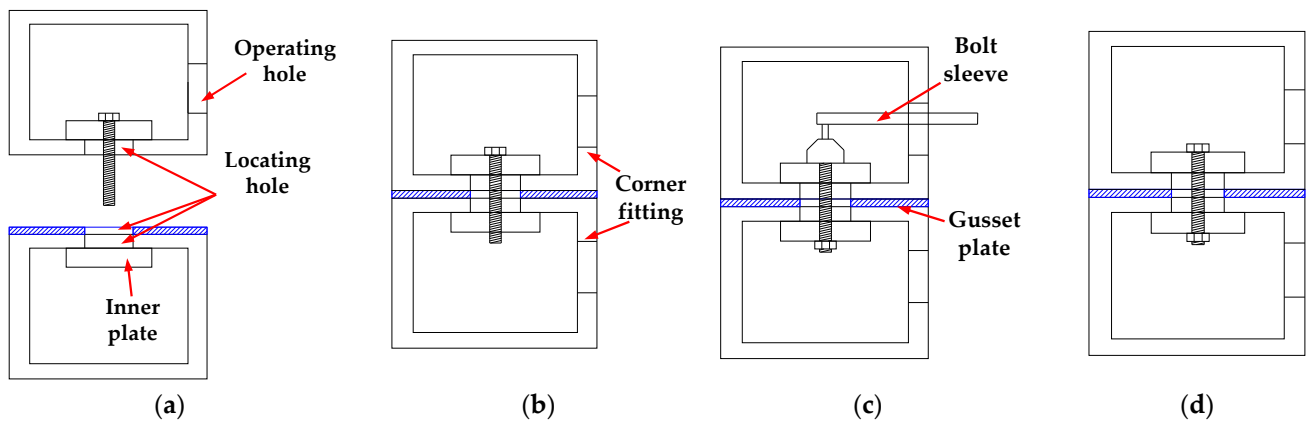


Figure 4. Diagram of the assembly process: (a) align vertically; (b) match locating hole; (c) fasten vertical bolt; and (d) complete connection.

Pretension load is applied to the long stay bolts. A 6 mm thick gusset plate is fastened to the upper and lower module components by a bolt connector. A 22 mm diameter high-strength bolt is employed to fasten the 10 mm thick internal plate in each corner fitting. The schematic of the bolt connector and corner fitting with its outer dimensions is presented in Figure 5. Three diameters of the long stay bolt (6 mm, 12 mm, and 16 mm) are considered to investigate the effect on the axial load-bearing capacity of the FPLC.

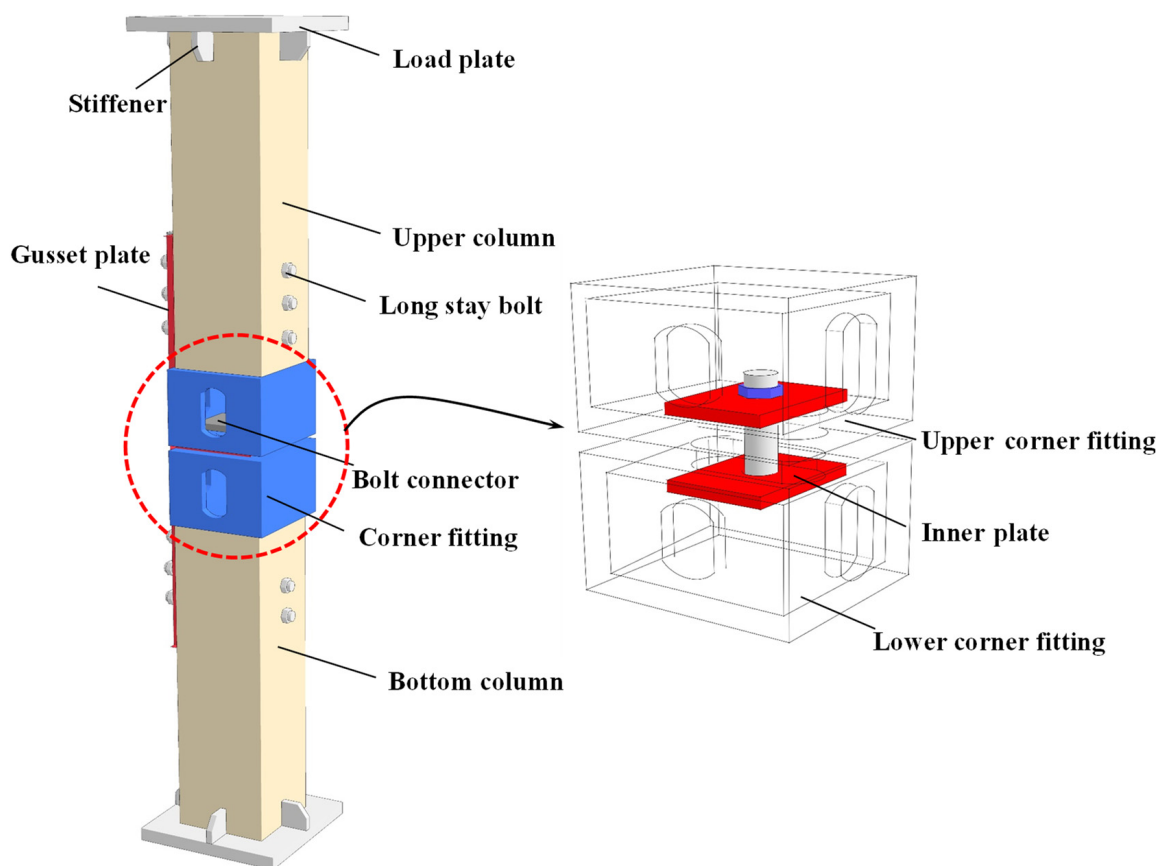


Figure 5. Schematic of the specimens.

3. Experimental Program

3.1. Specimen Design

Five full-scale specimens were designed in this paper. The diameter and number of long stay bolts were considered as parameters. Specimens were designed with various parameters and dimensions mostly used in engineering practice, as listed in Table 1. Aiming to better understand the behavior of FPLC with different diameters and numbers of long stay bolts when the specimen was subjected to axial compression, a 6 mm thick T-gusset plate and $150 \times 150 \times 6$ mm HSS column were adopted for all specimens. The reason to use the section size of an HSS column is that it has been extensively used in steel structures in China and is appropriate for standardization. The average measured thickness of the HSS column was 5.86 mm. Steel coupons were prepared following the requirements of GB/T228.1-2010 [35], as shown in Figure 6a. The average mechanical properties are listed in Table 2. The corresponding tensile stress-strain curve for the steel was presented in Figure 6b. In this study, the ultimate strength is considered as the maximum stress that the coupon exhibited and the yield stress is the strength at the inception of plastic strain of the stress-strain curve [36]. The geometric details of the test specimens are shown in Figure 7. The axial compressive load is transferred to the contact surface between the column ends and the corner fitting. The long stay bolts fasten the gusset plate and column. If the failure occurs near the bolt hole, bolts will also suffer shear force. In this way, the load capacity may increase.

Table 1. Summary of the test specimens.

Specimen	d/mm	n	l/mm
SC-1	6	2	448
SC-2	6	6	648
SC-3	12	6	648
SC-4	16	6	648
SC-5	6	10	848

Notes: d denotes the diameter of the long stay bolts; n denotes the number of the long stay bolts; l denotes the length of the gusset plate.

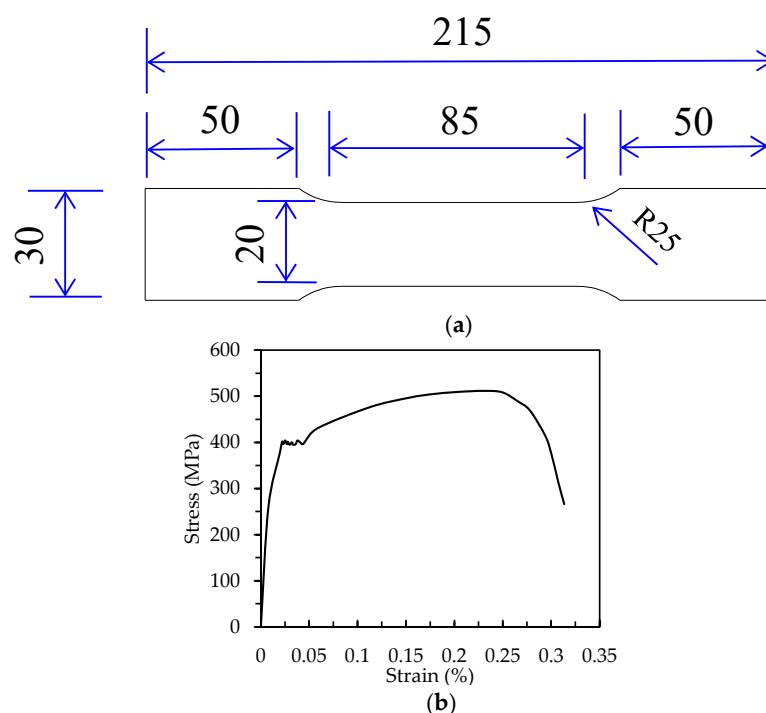


Figure 6. Design and results of material property test: (a) the nominal size of coupon specimen; (b) stress-strain curve.

Table 2. Material properties of the specimens.

Components	Yield Strength/MPa	Ultimate Strength/MPa	Elongation
HSS members and gusset plate	394	500	23.2%
Long stay bolt	640	800	5.0%
High-strength bolt	660	930	5.0%
Corner fitting	310	490	-

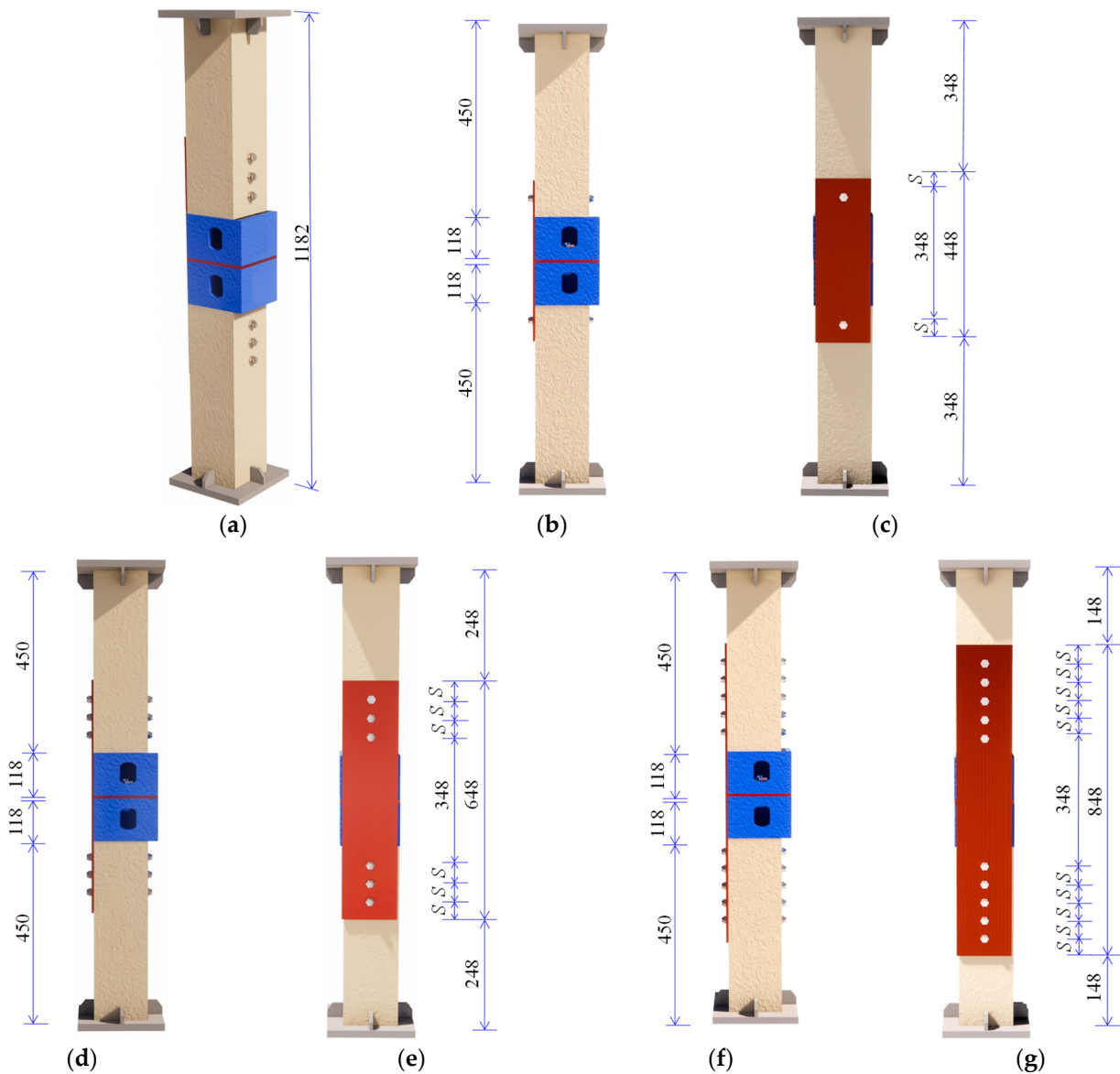


Figure 7. Design of the test specimens (all dimensions in mm): (a) 3D view of Specimen SC-2; (b) front view of Specimen SC-1; (c) side view of Specimen SC-1; (d) front view of Specimen SC-2~SC-4; (e) side view of Specimen SC-2~SC-4; (f) front view of Specimen SC-5; and (g) side view of Specimen SC-5. $S = 50$ mm is the space of the long stay bolt.

3.2. Test Setup and Loading

In this section, five monotonic axial compressive tests were conducted in the Structural Laboratory of Zhengzhou University. The schematic diagram of the test is shown in Figure 8a and the laboratory test setup is shown in Figure 8b. The test specimen was supported through baseplates at the ends of both columns to ensure full contact between

the specimens, load sensor, and support plates. The axial compressive load was performed by a hydraulic actuator at the bottom of the specimen. Meanwhile, the upper beam and frame columns were employed to restrain the vertical movements of the specimens.

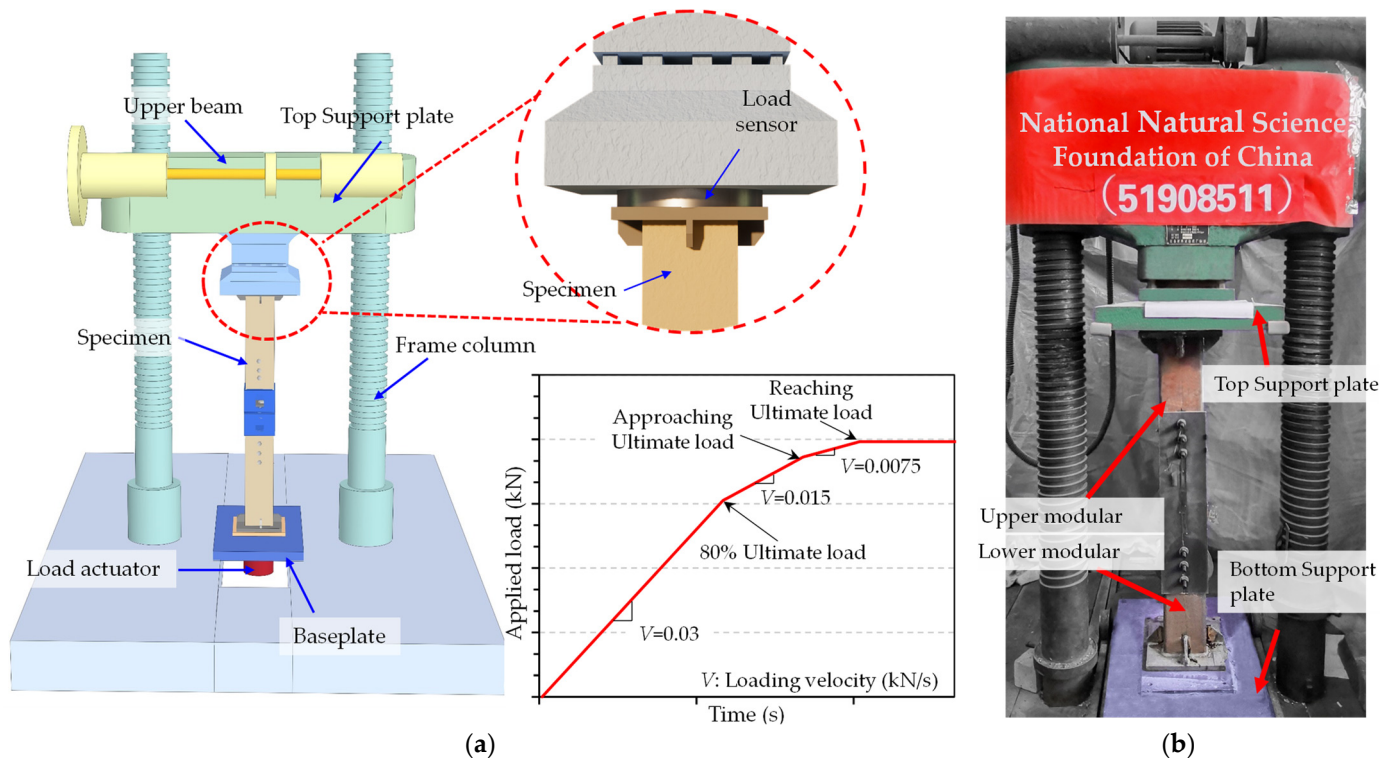


Figure 8. Test schematic of the FPLC under axial load: (a) schematic diagram; (b) on-site photo.

The test setup was designed considering the axial design force of the specimens. The specimens were loaded monotonically until the failure occurred. The specimen was placed on the bottom support plate. To ensure no eccentricity at the contact interface between corner fitting and gusset plate, the stiffeners on the specimen should be aligned with the four orientations of the cross graticule in the support plate. The loading protocol was designed based on Chinese code JJF 1296.2-2011 [37]. The loading increment at formal loading was taken as 5% of the estimated ultimate load of the specimen and the loading rate was 0.03 kN/s. The applied load versus the time relationship is shown in Figure 8. When the specimen underwent local buckling or the load reached 80% of the estimated ultimate load of the specimen, the incremental value of the load was halved. When the load was close to the estimated ultimate load of the specimen, the load increment was halved again. The loading was continued until the load dropped to about 75% of the ultimate load-bearing capacity of the specimen or a large visible deformation occurred with a tendency for overturning, and the test was terminated. The end of the top column was restrained from translating and rotation in all directions. The end of the bottom column was allowed to move only in the vertical direction.

3.3. Layout of the Measuring Points

Four linear variable differential transducers (LVDTs) were installed at the corners of the end plate of the bottom column, respectively. Other four LVDTs were installed on the specimens to measure the horizontal deformation of the specimens, as shown in Figure 9a–c. LVDT 1 and LVDT 2 were connected to the upper and lower columns between the gusset plate and the load plate, respectively. These two LVDTs were used to measure the possible out-of-plane deformation of the column. LVDT 3 was connected between the upper and lower corner fitting. LVDT 4 was connected to the middle of the gusset plate. These two

LVDTs were used to measure the relative movement of the specimens. It should be noted that LVDT 2 was not installed for Specimen SC-5 because the free end of the column was too short.

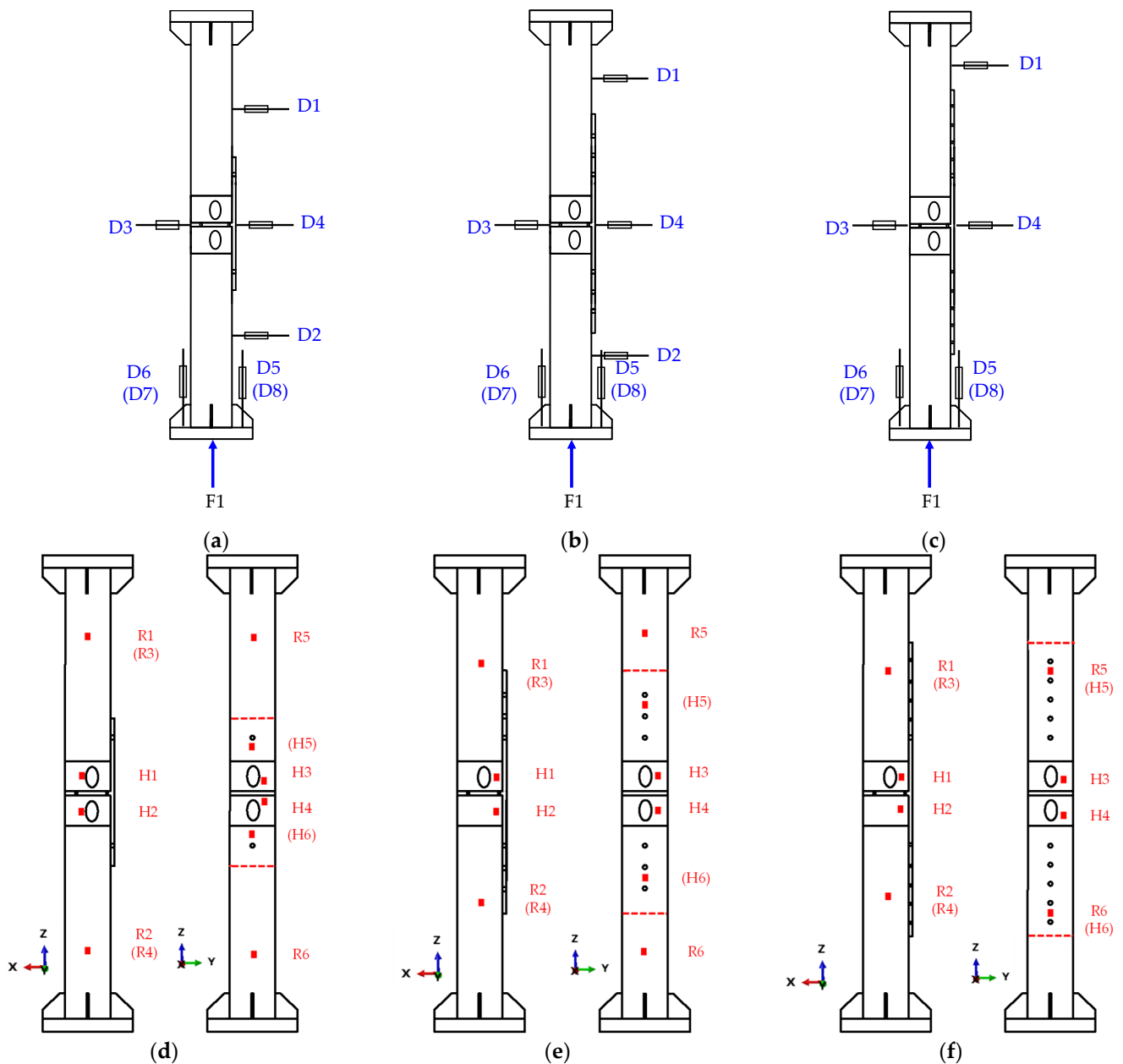


Figure 9. Layout of transducers: (a) locations of LVDTs for SC-1; (b) locations of LVDTs for SC-2~SC-4; (c) locations of LVDTs for SC-5; (d) SC-1 strain gauge measurement; (e) SC-2~SC-4 strain gauge measurement; (f) SC-5 strain gauge measurement. Notes: R denotes strain rosette; H denotes strain gauge; () denotes strain gauge was attached to the reverse side.

A total of 11 strain gauges were attached at different locations of the components where local buckling was estimated to occur, as shown in Figure 9. R1, R3, and R5 were attached to the middle-height of the upper column and R2, R4, and R6 were attached to the symmetric locations on the lower column. To monitor the strain distribution of the corner fitting, H1, H2, H3, and H4 were attached near the openings on the corner fitting. H5 and H6 were installed near the bolt hole where strain concentration may be anticipated.

4. Experiment Results and Analysis

4.1. Failure Mode

All five specimens presented deformation before failure. Out-of-plane deformation occurred on the HSS columns when the ultimate load was reached. The local buckling was generally located at the middle or at the quarter length of the column. There was no obvious deformation at the beginning of the loading for all specimens. As the loading continued, the axial displacement increment increased, implying that the specimen entered an elastic-plastic stage. When the load reached 90% of the ultimate load-bearing capacity of the specimens, columns experienced significant local buckling. When the load reached the ultimate load-bearing capacity of the specimen, the buckling of the specimen continued to increase, leading to failure of the specimen. Meanwhile, the load began to decrease, and the test was terminated when the load dropped to about 75% of the ultimate bearing capacity of the specimen. It should be noted that the test was terminated early for Specimen SC-3 because the specimen appeared to have a visible tendency for overall instability.

The deformations of Specimens SC-2, SC-4, and SC-5 were exhibited near the long stay bolts. In this way, the bolts bear part of the shear force, resulting in the increase of the ultimate load. The failure mode of Specimen SC-1 was presented in Figure 10a. Specimen SC-1 experienced local buckling at the quarter of the lower column. The final damage of Specimen SC-2 and Specimen SC-4 was similar, as shown in Figure 10b,d. Local buckling was located at the middle of the column, which was near the bolt hole. For Specimen SC-2, the bolts experienced damage to different degrees because it suffered shear force. The final damage of Specimen SC-5 was similar to that of Specimen SC-2 and Specimen SC-4 was expected to have local buckling obvious near the bolt hole and the bolt suffered shear force, as shown in Figure 10e. Different from other specimens, global instability occurred for Specimen SC-3, as shown in Figure 10c. Nonetheless, the failure mode of Specimen SC-3 was in essence local buckling. In other words, local buckling occurred on the column early, leading to the overall instability of the specimen.

4.2. Load-Displacement Curve Analysis

Figure 11a shows the load-displacement curves of the specimens with different bolt numbers. Figure 11b presents the comparisons of the ultimate load and yield load for Specimens SC-1, SC-2, and SC-5. In this paper, the ultimate load is considered as the maximum capacity of axial compressive load and yield load is the load at the inception of plastic strain. It can be concluded from Figure 11 that the load-bearing capacity may decrease when the number of long stay bolts increases. The ultimate load increases by 11.74% and 2.79% for Specimens SC-2 and SC-5, respectively, compared to that of Specimen SC-1, as shown in Figure 11c. The local buckling occurred at the quarter of the column for SC-2 and SC-5 where long stay bolts suffered the shear force. In this way, the ultimate load of SC-2 and SC-5 is higher than SC-1, as shown in Figure 11a. The number of bolt holes of SC-5 is more than that of SC-2. In other words, the total area of bolt holes of SC-5 is larger than that of SC-2, which weakens the columns. Therefore, the ultimate load of SC-2 is higher than that of SC-5.

Figure 12a presents the load-displacement curves of the specimens with different bolt diameters. Figure 12b,c show the relationship between bolt diameters and the reduction in yield and ultimate load capacities. These figures indicated that with the increasing of the bolt diameters on the column, the ultimate load and yield load apparently decreased. Compared to Specimen SC-2, the axial compressive-load capacity of Specimen SC-3 decreased by 10.06%. Considering the randomness of the location of local buckling, the long stay bolts could not contribute much to the compressive resistance of the specimens if the local buckling did not occur near the long stay bolts. In this way, the strength of the column was weakened, resulting in the decrease of the compressive resistance of the specimen. A similar phenomenon could be captured for Specimen SC-1, as shown in Figure 10. The axial compressive-load capacity of Specimen SC-4 with bolt holes of 16 mm decreased by 15.09% compared to Specimen SC-2 with bolt holes of 6 mm. This is because the shear strength

of the bolt with a diameter of 16 mm is greater than the bearing strength of the bolt hole. The diameter of the bolt hole of Specimen SC-4 was larger than that of SC-3, which further weakened the strength of the column.

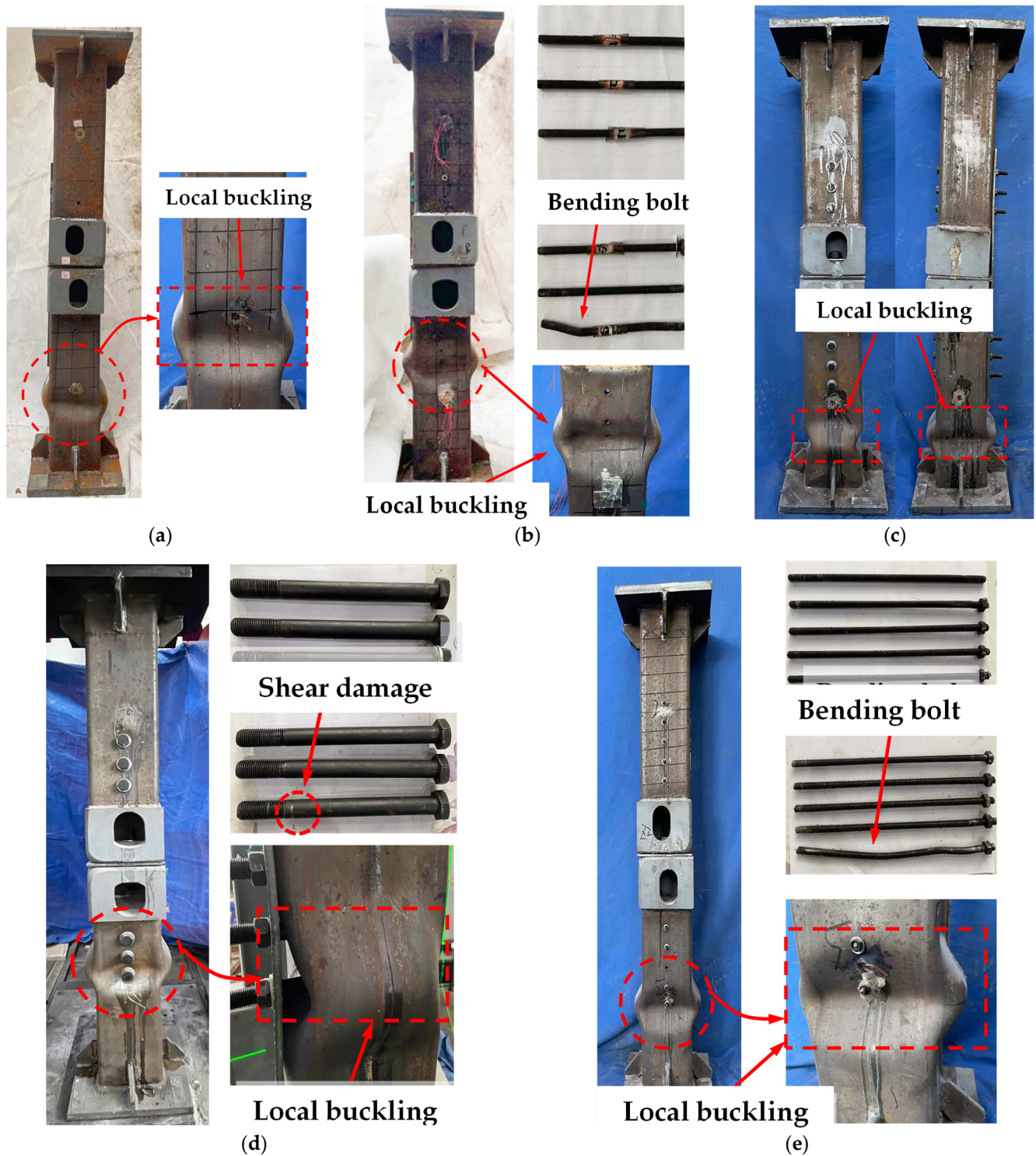


Figure 10. Failure mode of the specimens: (a) Specimen SC-1; (b) Specimen SC-2; (c) Specimen SC-3; (d) Specimen SC-4; and (e) Specimen SC-5.

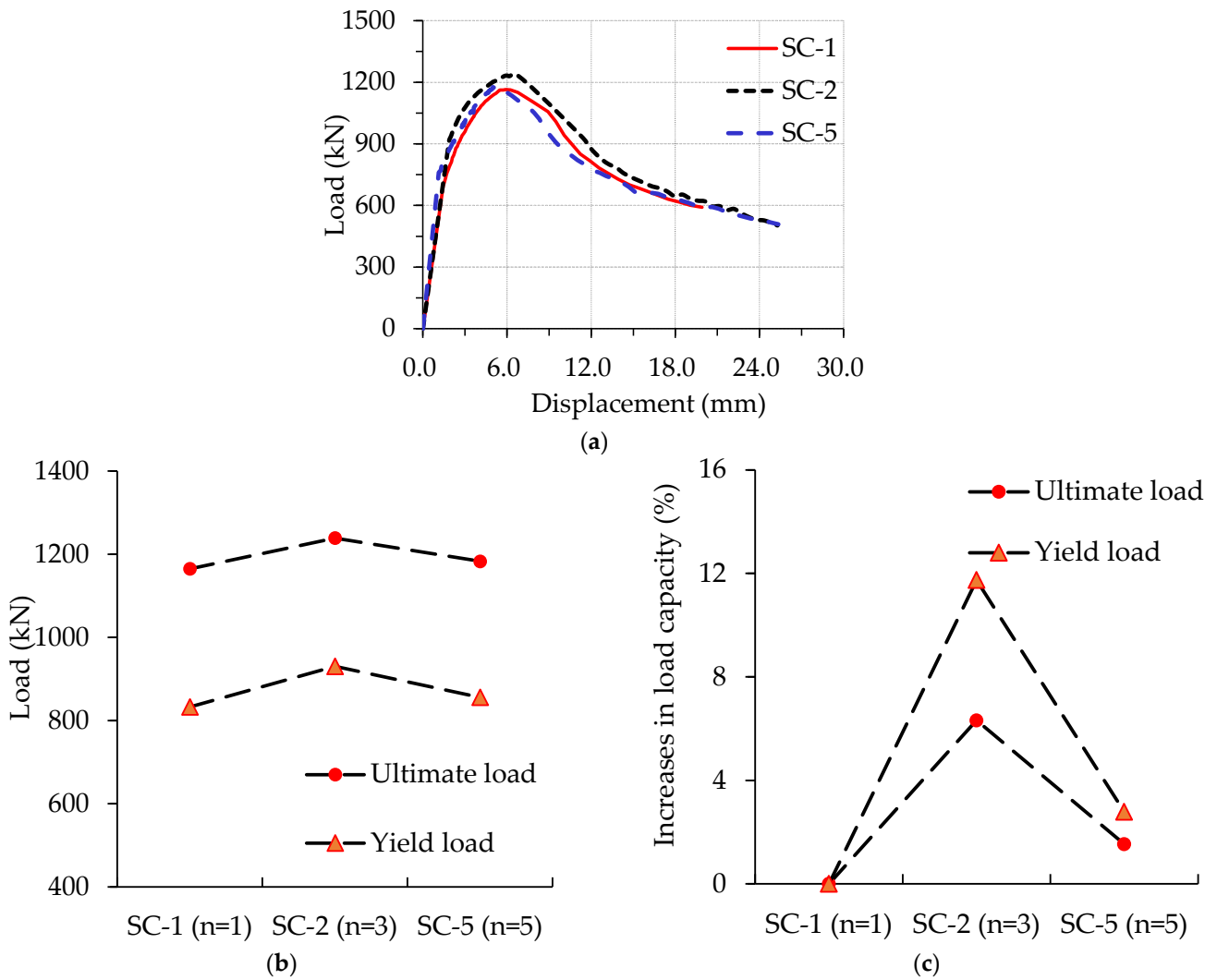


Figure 11. Comparisons of specimens with different bolt number: (a) comparisons of load-displacement curves with various bolt numbers; (b) yield load and ultimate load with various bolt numbers; and (c) percentage variation of load capacity with various bolt numbers.

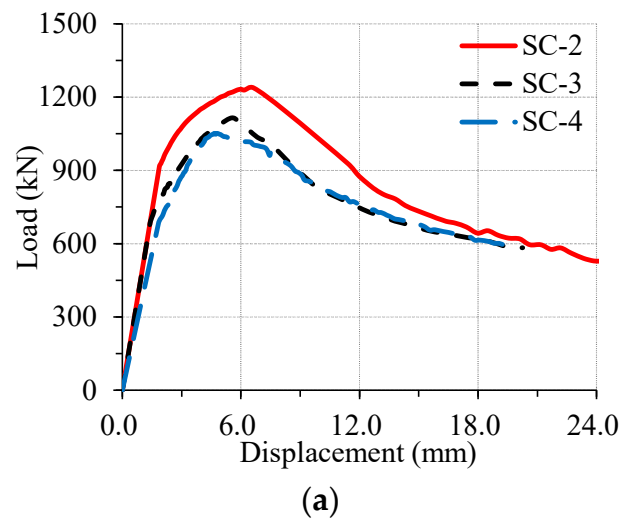


Figure 12. Cont.

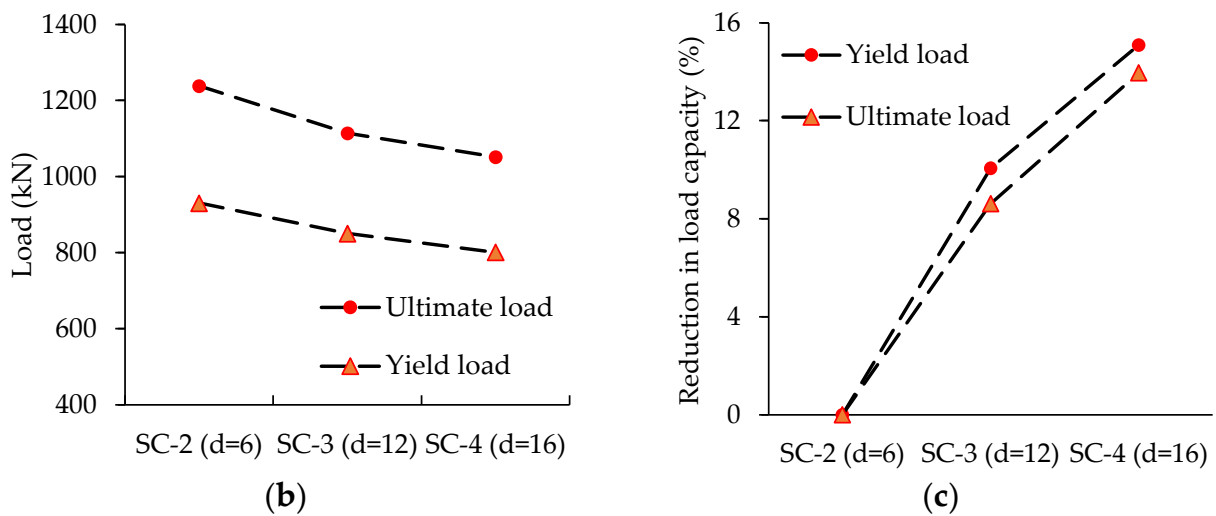


Figure 12. Comparisons of specimens with different bolt diameters: (a) comparisons of load-displacement curves with various bolt diameters; (b) yield load and ultimate load with different bolt diameters; and (c) percentage variation of load capacity with various bolt diameters.

4.3. Strain Distribution and Development

The load-strain behaviors of the specimens were investigated by the three representative Specimens SC-1, SC-2, and SC-5. Three strain gauges were picked for the three specimens, two at the top column and one at the lower column. The strain-displacement curves of the specimens are shown in Figure 13a–c, respectively. The strain data corresponding to ultimate load of the specimens were picked, as shown in Figure 13d–f, respectively. It should be noted that ϵ_y denotes the yield strain of steel.

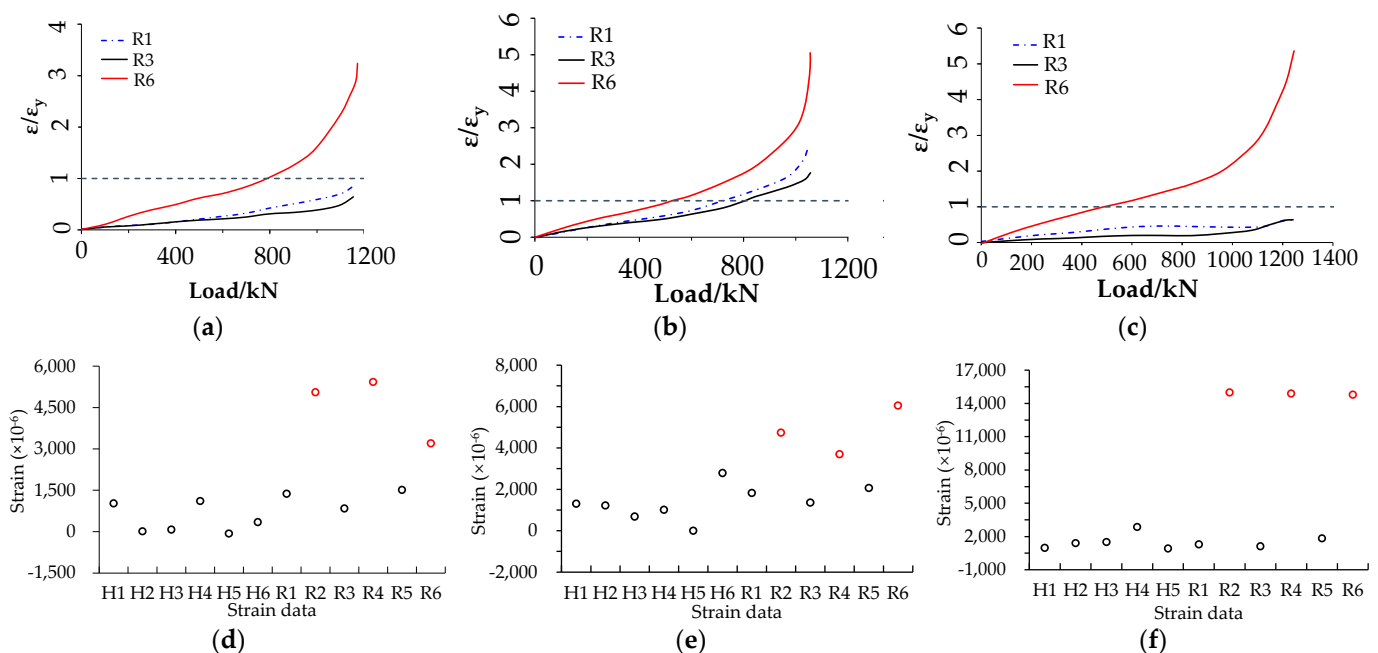


Figure 13. Strain gauge values obtained from the test: (a) strain-load curves of Specimen SC-1; (b) strain-load curves of Specimen SC-2; (c) strain-load curves of Specimen SC-5; (d) strain data of Specimen SC-1; (e) strain data of Specimen SC-2; and (f) strain data of Specimen SC-5.

It can be concluded from Figure 13 that the strain on the column increases quickly after the maximum load. A further increase of the axial load causes local buckling in the HSS column. It can be observed that the top column almost remained elastic during the

test. These figures showed that stress concentration occurred mainly at the locations of local buckling and the openings of the corner fittings.

5. Development and Validation of Finite Element Model

5.1. General

The full-scale testing of the specimens has provided key information about the axial compressive performance of the FPLC. However, finite element models (FEM) could provide a better understanding of the load-transferring mechanism that could not be obtained by physical tests. In this paper, the ABAQUS/Standard version, distributed by SIMULIA Inc. [38], was applied to develop the three-dimensional nonlinear FEM of the test specimens. Material, geometric, and contact nonlinearities were modeled. The elastic-plastic material model employing multilinear kinematic hardening principles was utilized for the cast-steel material [39]. On the other hand, the isotropic hardening principles and Mises yield criterion were employed for other members of the connection. The elastic modulus of steel was taken as 2.06×10^5 MPa, and Poisson's ratio was taken as 0.30. The corresponding characteristic values of the materials are presented in Table 2.

5.2. Element Type, Boundary Condition, Mesh, and Loading

The FEM developed in this study for Specimen SC-2 is shown in Figure 14. All the components were modeled using C3D8R-type solid elements. It has been proven to be a reliable element for investigating the mechanical characteristics of structures, connections, and components [13,19,40]. The welded components in the connection were modeled using the "Tie" constraint, including the column end to the base plate and stiffener to the base plate. The "tied" components moved together with the same displacement and rotation. The column and the corner fitting were merged to reduce complex interactions in the developed FEM. A surface-to-surface hard contact interaction with a friction coefficient of 0.3 was employed to simulate the contact interfaces, including bolt to bolt hole, bolt nut to column wall, bolt nut to gusset plate, bolt nut to inter slab, inter slab to corner fitting, and so on.

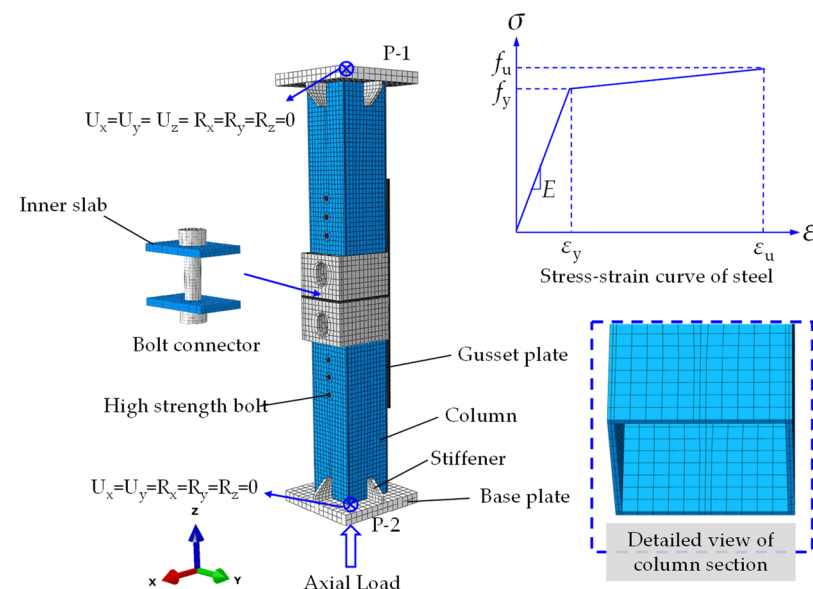


Figure 14. FEM of experimental specimens.

Figure 15 plots the effect of mesh size on the numerical results of representative Specimen SC-2. It shows that the varying mesh size has a quite limited influence on the elastic stage of the load-displacement curve obtained by FEA of the FPLC. This varying mesh size does influence the ultimate compressive capacity and stiffness within 5%. However, the FEM with a coarse mesh mismatched the experimental results after the specimen reached

ultimate load. Furthermore, it confirmed that fine and intermediate mesh sizes offer better numerical results. Considering the computing efficiency, the finite element model with an intermediate mesh size was applied in subsequent investigations. The element sizes are 4 mm for bolts, 12 mm for columns, 15 mm for corner fittings, 20 mm for loading plates, 8 mm for inter slabs, and 15 mm for gusset plates. The mesh was encrypted along the thickness of the components, as shown in Figure 14.

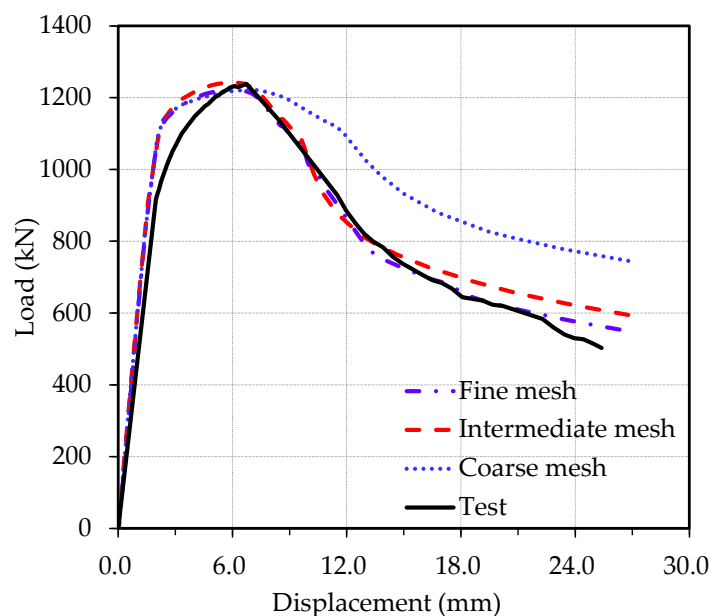


Figure 15. Effect of different mesh sizes on finite element simulation results.

Applying preload to the high-strength bolt by “bolt load” mainly included two steps: (1) applying the preload along the axis of the bolt to simulate a fully tightened state of the bolt; and (2) fixing the axial length of the bolt. The base plates were kinematically coupled to the reference points for distributing the concentrated load and applying the boundary conditions. Rotation and translation were constrained in the X, Y, and Z axes for Point-1 (P-1). Rotation in the X, Y, and Z axes and translation in the X and Y axes were constrained for Point-2 (P-2). Axial displacement was applied at Point-2 (P-2). In this way, the axial force-displacement curve can be obtained, and the FEM can simulate the axial behavior of the connection. It should be mentioned that initial imperfection was considered in each specimen. The eigenvalue analysis is necessary prior to the axial loading to introduce the initial geometric imperfection. Such an analysis is a linear elastic analysis performed using the (*BUCKLE) procedure available in the ABAQUS library [41]. $l_e/1500$ is available for axial flexural geometric imperfection of the columns [42]. l_e denotes the effective length of the column.

5.3. Verification of the FEM

The comparison of the load-displacement curves between the FEM and test results is presented in Figure 16. The initial gaps in the specimens were not considered in the FEM. Therefore, the elastic stiffness was slightly higher in the FEM than in the test. A comparison of ultimate load and stiffness for specimens in the experiments and the FEA results are shown in Figure 16f. In addition to the fluctuation of the individual results, most of the scattered points are centered around value 1. The comparisons suggest that the FEM can reasonably predict the axial compressive behavior of the FPLC. Initial stiffness, the ultimate load, and post-buckling behavior can be accurately predicted by the FEM. The difference between the FEM and test results is less than 3.5%, which further verifies the reliability of the FEM.

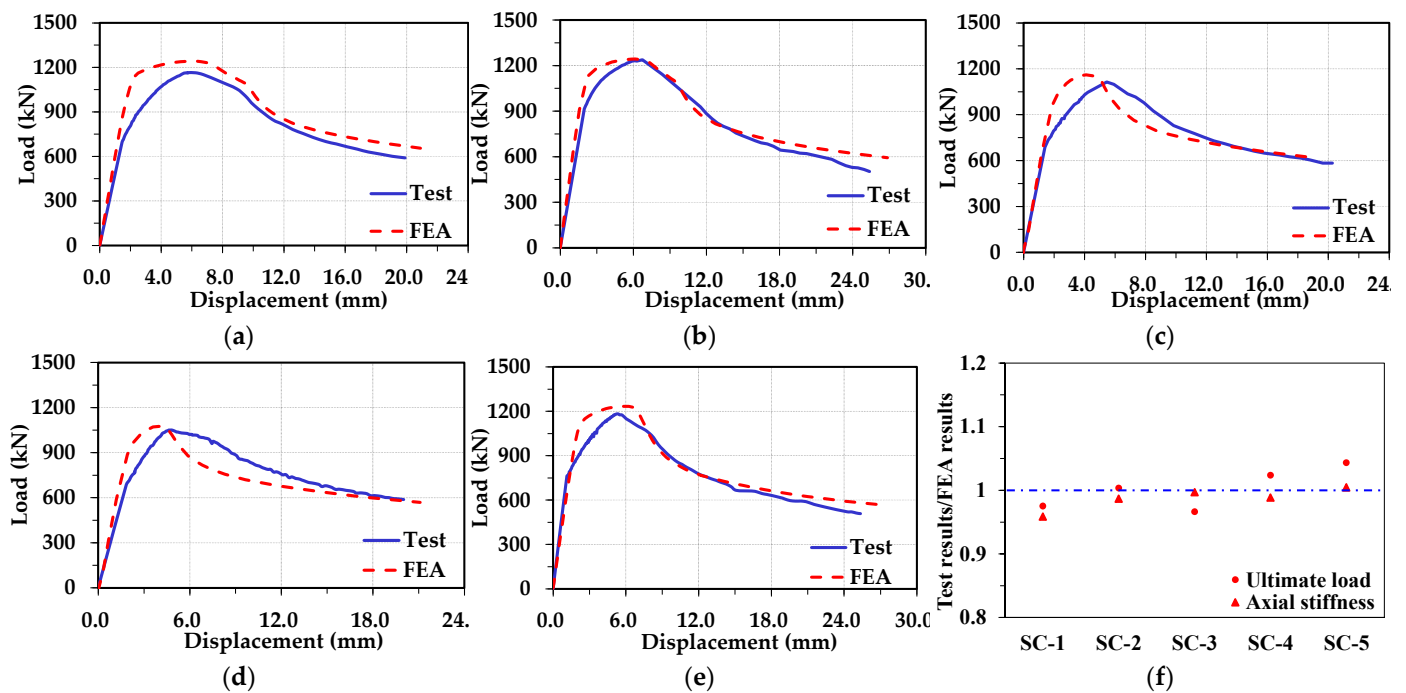


Figure 16. Comparisons of load-displacement curves: (a) Specimen SC-1; (b) Specimen SC-2; (c) Specimen SC-3; (d) Specimen SC-4; (e) Specimen SC-5; and (f) comparisons between results of FEA and tests.

The failure mode is also a critical evaluation criterion for the FEM. Figure 17 shows a comparison of the failure mode between the test and the FEA for Specimen SC-3. The out-of-plane deformation of the column in the test and the FEA was similar. Due to the randomness of the buckling locations, accurate results were difficult to obtain in the numerical simulation. The analysis indicated that the failure process of the test and the FEA was consistent. It can be observed from Figure 17 that the high-level stress was concentrated at the lower modular column, where severe buckling deformation caused by axial load was obvious. Compared with the lower modular column, the upper column had a lower stress level. For the connecting components, such as corner fittings and bolt connectors, the Von Mises stress level was found to be within a relative safe range. The FPLC can provide reliable force transmission between components and meet the demand for a “strong joint and weak member”.

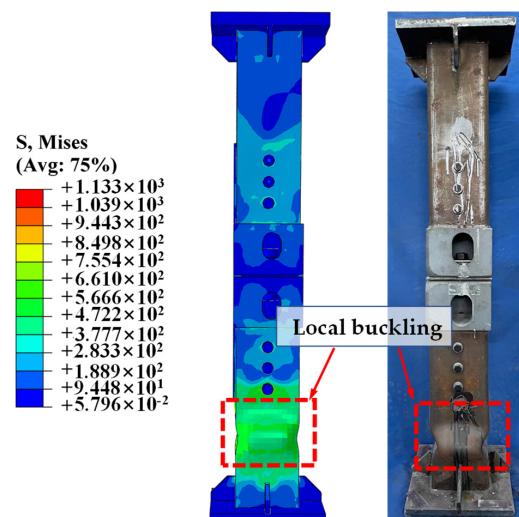


Figure 17. Comparison of failure mode.

6. Parametric Study

In this section, the validated FEM was adopted to conduct the parametric analysis to reveal the influence of the geometric parameters on the axial compressive performance of the FPLC.

6.1. Details of the Parameters

According to the failure mode investigated above, the failure of the specimens was caused by the local buckling of the column rather than the corner fitting. Therefore, an optimization of the corner fitting is needed. In this way, the weight of the corner fitting, the location of the column, and the strength, length, and thickness of column were considered as parameters to conduct the parametric study. Table 3 lists the values of the parameters considered in the parametric study. The weight reduction (WR) of the corner fitting introduced in this table is calculated with respect to the specimens tested in this paper. It should be noted that the "0 WR" denotes the original thickness of the corner fitting. The WR of the corner fitting was achieved by reducing the thickness in three dimensions. The models are identified with the notations introduced in Table 3. Three different locations for the column were considered, as shown in Figure 18. The values presented in Table 3 represent the changes in the location and section of the column. The specimens with different strengths and lengths of the column were based on the verified FEM of Specimen SC-4. In total, 53 FEMs were considered in the parametric study.

Table 3. Values of the parameters.

Parameter	Values	Notation
Weight reduction (WR) of the corner fitting	0%, 5%, 10%, 15%, and 20%	0 WR, 5 WR, 10 WR, 15 WR, and 20 WR
Locations of the column	0, 14 mm, and 28 mm	Original, Middle, and Corner
Thickness of the column	6 mm, 8 mm, and 10 mm	6 TC, 8 TC, and 10 TC
Material properties of the column	Q355, Q390, Q420, and Q460	-
Length of the column	450 mm and 700 mm	-

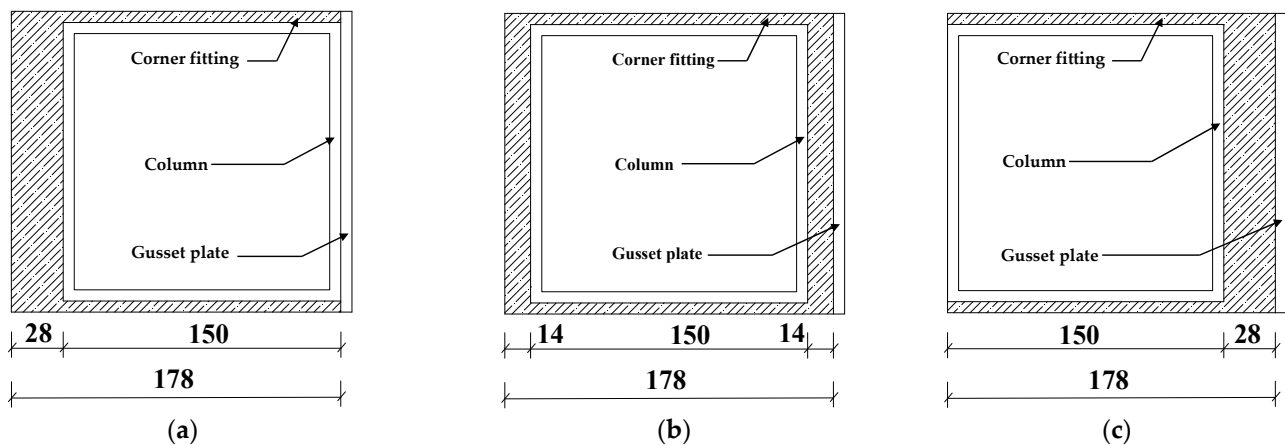


Figure 18. Locations of columns on the corner fitting: (a) original location; (b) middle location; and (c) corner location.

For a better understanding of the internal stress distribution and plasticity within the connection components, the Von Mises stress and equivalent plastic strain (PEEQ) values at some key points were obtained from the FEM when the ultimate load was reached, as shown in Figure 19a–c. PEEQ could value the accumulative results of plastic strain, which was employed in this paper to determine the main bearing components of the connection. U1, U2, L1, and L2 were around to the opening on the corner fitting. If damage occurred on the corner fitting, obvious deformation mainly occurred at the opening of the corner fitting. C1 and C2 were near the contact interfaces between the column and the corner

fitting. These were the representative points with high stress values. The specific locations of the reference points were decided based on the mesh size of the FEM.

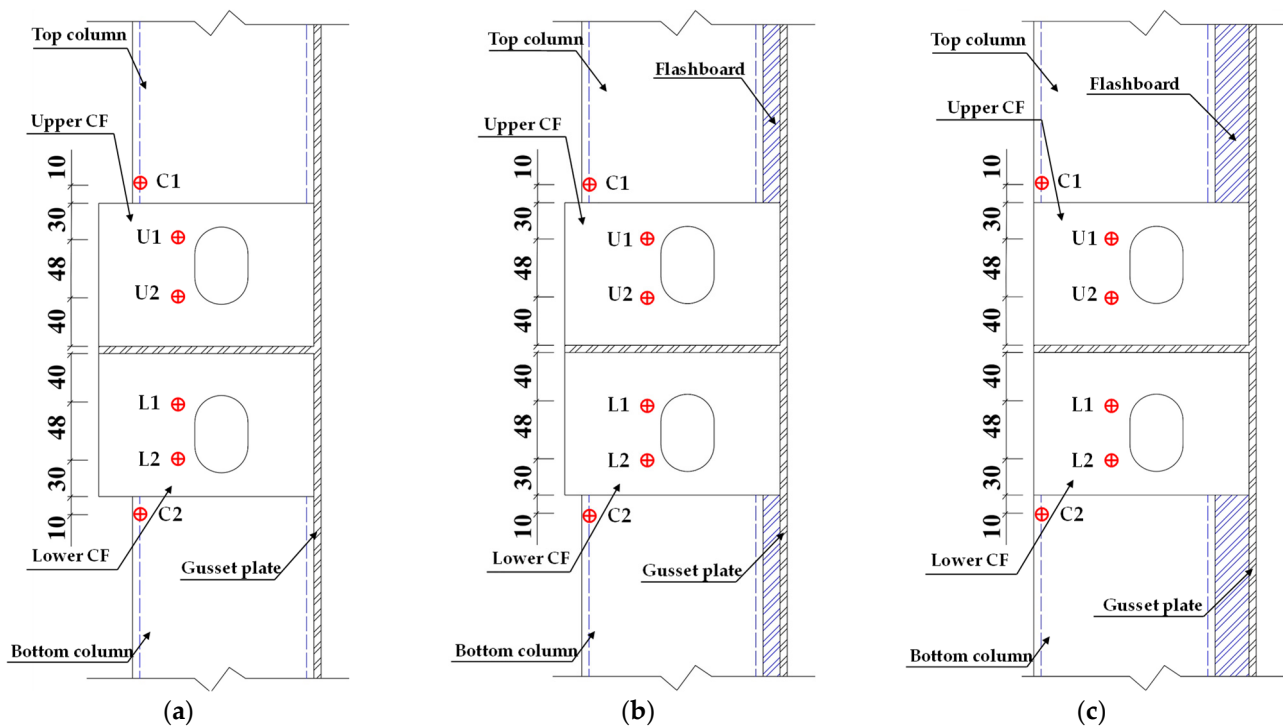


Figure 19. Reference points and column location: (a) reference points of original column location; (b) reference points of column location in middle of the corner fitting; and (c) reference points of column location in corner of the corner fitting.

6.2. Effect of Location of the Column

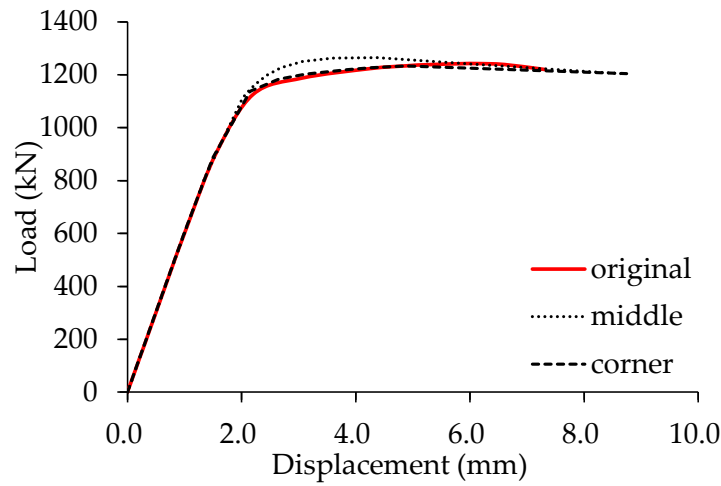
Figure 20 shows the influence of different locations of the column on the ultimate load of the FPLC. It can be found that the column location does not affect the axial load-bearing capacity of the connection if the thickness of the column and weight of the corner fitting remained the same, as shown in Figure 20a. As the column is located off the opening of the corner fitting, the stress distribution in the column reduces and the stress in the corner fitting increases, as shown in Figure 20.

Moreover, stress in columns is always higher than in the corner fitting. As the column becomes thicker, the values of PEEQ distribution in the corner fitting increased. A high value of PEEQ indicates that the corner fitting has already been damaged before the specimen reached the ultimate load. Since the PEEQ value of Point U-2 and L-1 on the corner fitting is much higher than other points, the corner column is unfavorable for the specimen with a column thickness of 10 mm, as shown in Figure 20g. It should be noted that the trend variation is due to the different behaviors of the material after yielding, as shown in Figure 20g. Besides, the values of stress and the PEEQ of models with the column located in the middle of the corner fitting are much higher than other locations for 10 TC models.

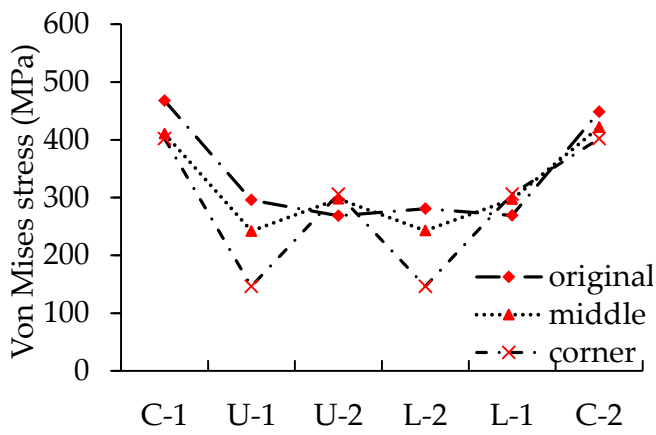
6.3. Effects of Weight Reduction of the Corner Fitting

Figure 21 presents the influence of the weight of the corner fitting, taking six TC-original models as examples. The ultimate load of the FEM increases as the corner fitting becomes thicker, as shown in Figure 21a. The corner fitting and the columns experienced axial deformation with the increase of axial load. After reaching the maximum load, inelastic buckling occurred at the columns. In all results of the FEA, the plastic strain first occurred at the columns. It can be observed from Figure 21b that the axial load-bearing

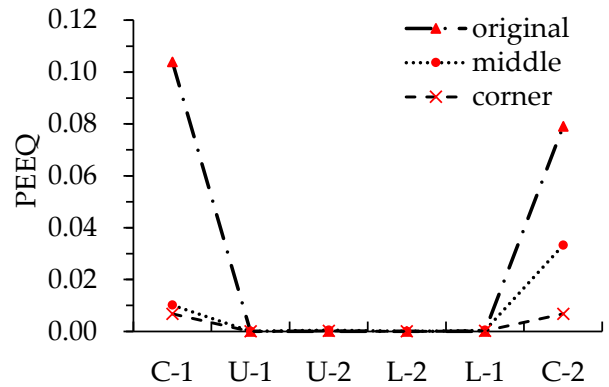
capacity decreased from 2% to 8% and the yield load decreased from 5% to 8.5% as WR increased from 5% to 15%. There is a dramatic decrease both in yield load and ultimate load with WR to be 20%.



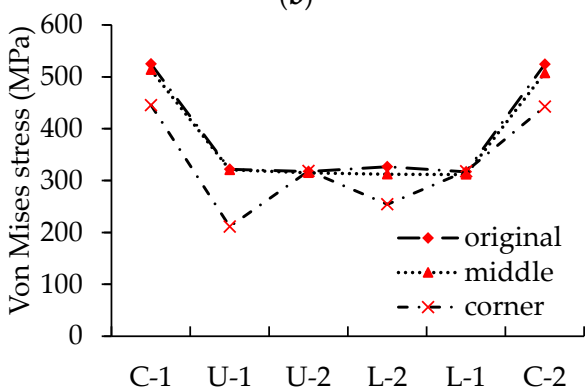
(a)



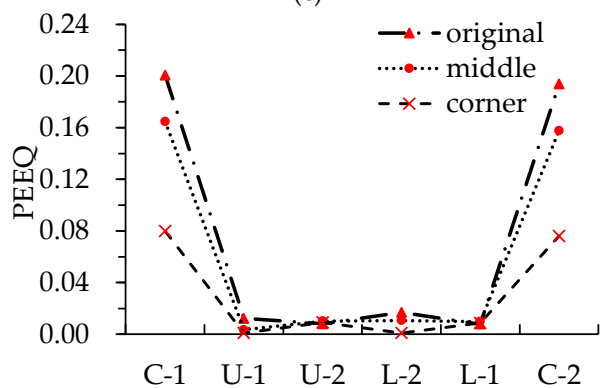
(b)



(c)



(d)



(e)

Figure 20. Cont.

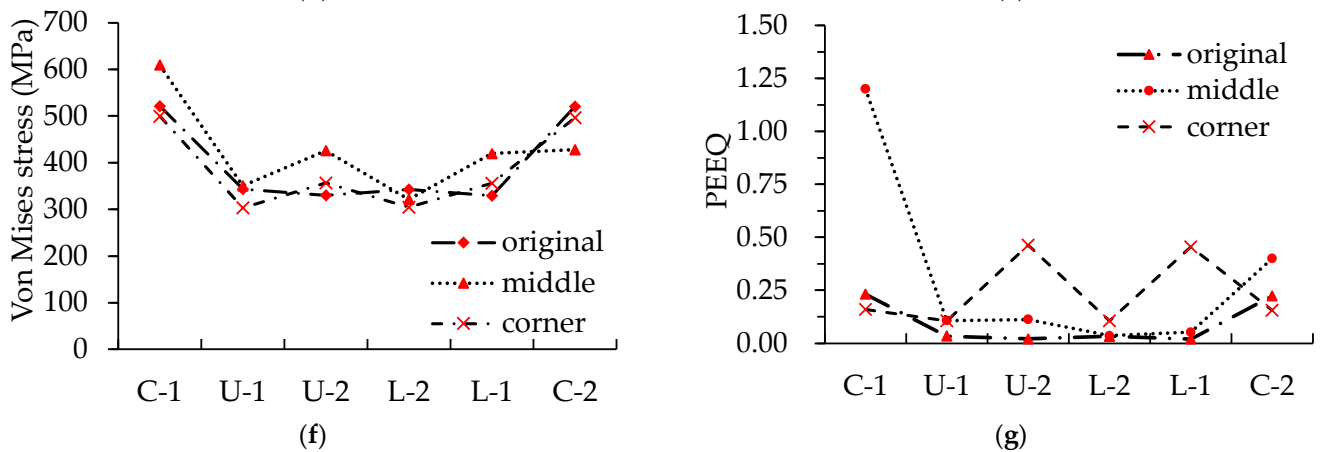


Figure 20. Comparisons of different column locations: (a) 6 TC models with 0% weight reduction; (b) Von Mises distribution of 6 TC with 0% WR model; (c) PEEQ distribution of 6 TC with 0% WR model; (d) Von Mises distribution of 8 TC with 0% WR model; (e) PEEQ distribution of 8 TC with 0% WR model; (f) Von Mises distribution of 10 TC with 0% WR model; and (g) PEEQ distribution of 10 TC with 0% WR model.

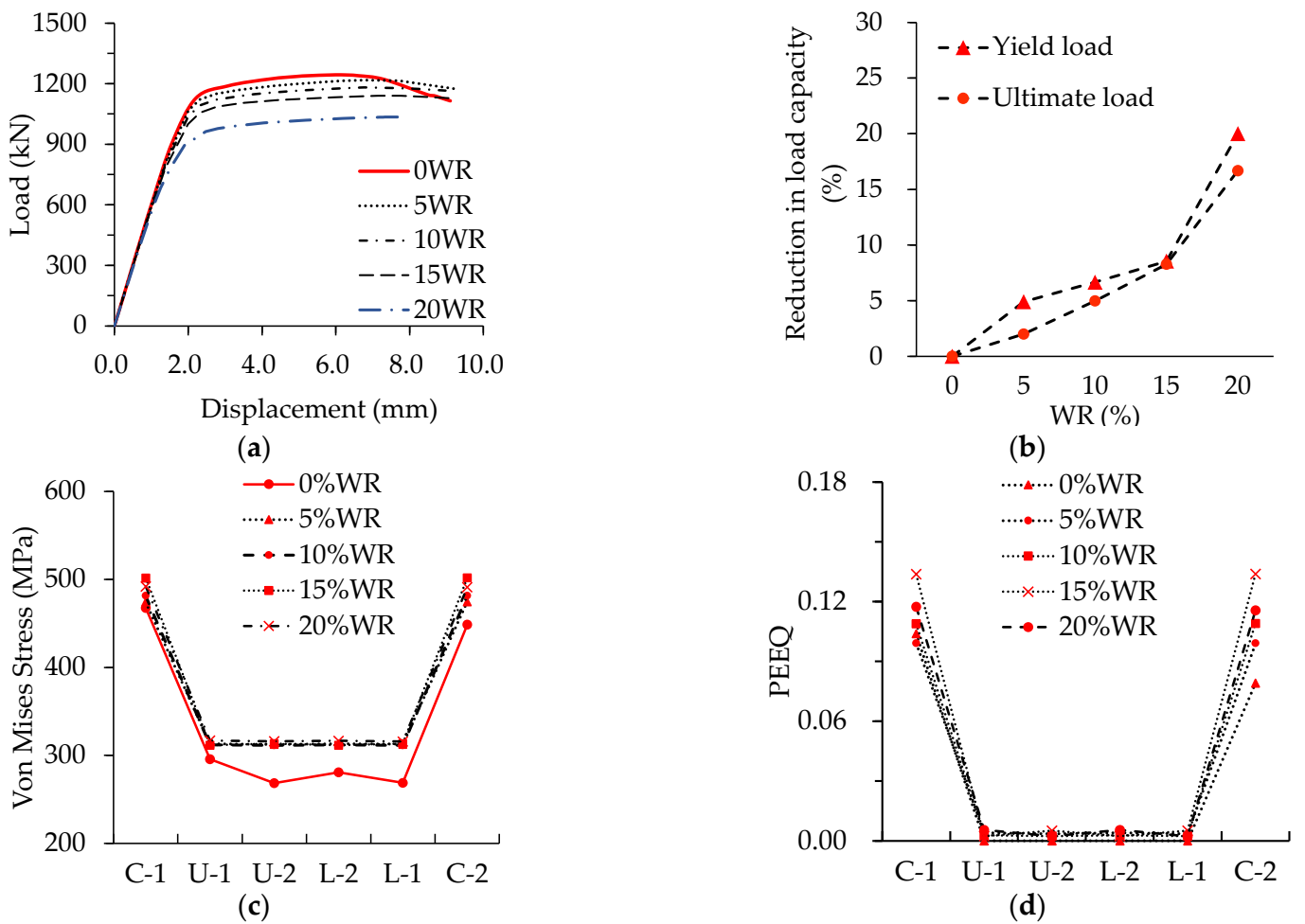


Figure 21. Comparisons of different weight of the corner fitting: (a) 6 TC and original models; (b) reduction in load-bearing capacity; (c) Von Mises distribution of original 6 TC model; and (d) PEEQ distribution of original 6 TC model.

Figure 21c,d present the relationship of the weight reduction of the corner fitting and the distribution of Von Mises stress and PEEQ in the connection. Stresses in the columns increased at first and decreased later for the 20 WR model. Therefore, the yield stage of the connection occurred, and yield and ultimate compressive-load capacity were reduced. With the weight reduction of the corner fitting increased, the PEEQ increased slightly. Therefore, the corner fitting may step into the plastic stage by decreasing its thickness. Stresses and PEEQ distribution in the corner fitting were more stable when WR varies from 5% to 20% compared to those in the columns. This is due to the different post-yielding nonlinear behaviors of the materials of the corner fittings and columns.

6.4. Effects of the Columns

Figure 22 depicts the influence of the length and strength of the columns on the ultimate compressive resistance of the FPLC (P). It shows that the ultimate load of the FPLC increases with the increase of the strength of the column. With the increases of the conditional yield strength of the columns from 355 MPa to 460 MPa, the increments of P for the connection with a length of 450 mm (700 mm) are 20.5% (19.8%), 30.3% (28.4%), and 42.4% (42.3%), respectively. The ultimate load of the FPLC is closely related to the strength and thickness of the column, i.e., the increased strength and the thickness of the column improved the cross-sectional compressive resistance of the connection. The reduction of P ranges from 1.8% to 3.3% when the length of the columns increases from 450 mm to 700 mm.

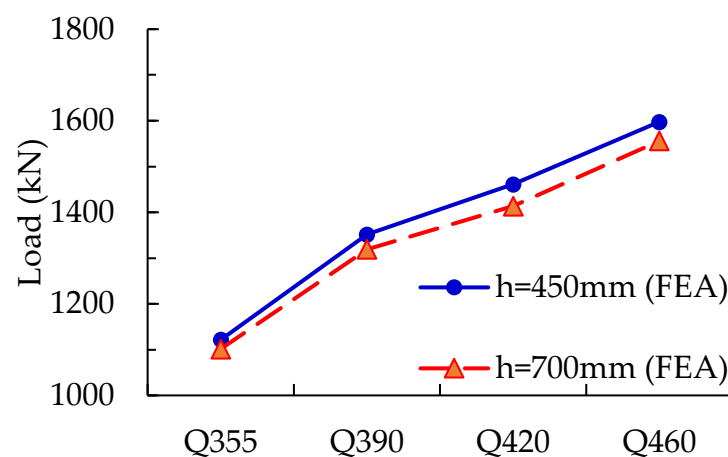
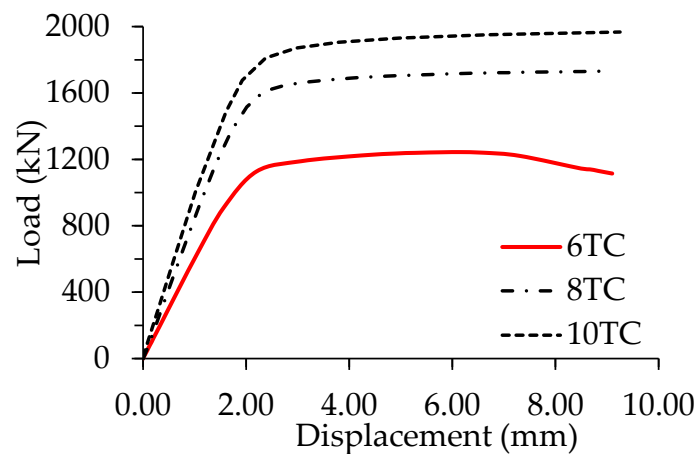


Figure 22. Comparisons of different lengths and strengths of the columns.

Figure 23 presents the influences of the thickness of the columns on the failure mode and ultimate load of the connection. The ultimate load of the FEM increased as the column became thicker. After reaching the inelastic bearing capacity, displacement kept increasing and load decreased slowly and inelastic buckling occurred on the column. As the thickness of the column increases from 6 mm to 8 mm and 10 mm, the ultimate compressive resistance of the FPLC increases by 55.4% and 77.7%, respectively, as shown in Figure 23a. The failure mode changes from local buckling to global instability, as shown in Figure 23b–d.

6.5. Summary and Discussions

The parametric studies showed that (1) changing the location of the column from original to the corner had limited influence on the compressive load capacity of the FPLC; (2) decreasing the weight of the corner fitting from 5% to 15% decreased the ultimate load capacity of FPLC from 2% to 8%; (3) increasing the strength grade of the column increased the ultimate load capacity of FPLC significantly; and (4) as the thickness of the column wall increased from 6 mm to 8 mm and 10 mm, the ultimate compressive resistance of FPLC increased by 55.4% and 77.7%.



(a)

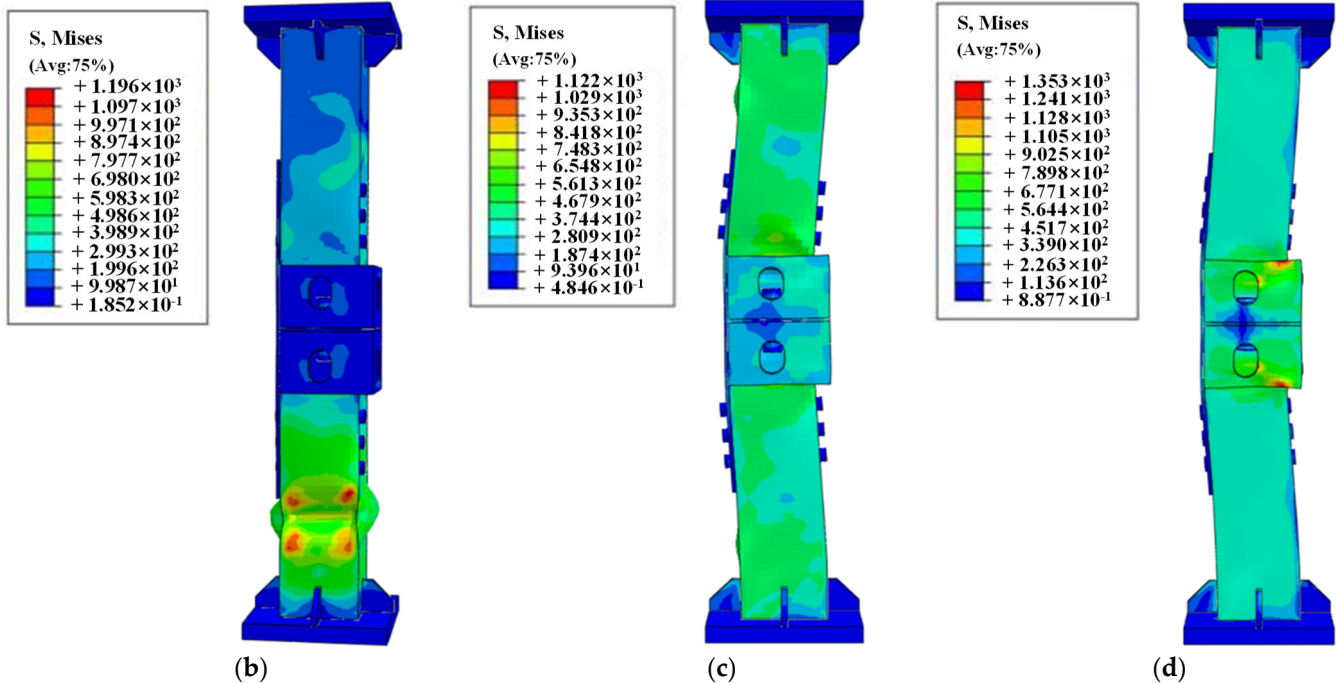


Figure 23. Comparisons of different thickness of the columns: (a) original models with 0% weight reduction; (b) failure mode of six TC model; (c) failure mode of 8 TC model; (d) and failure mode of 10 TC model.

The results of the parametric studies showed that to satisfy the requirement of uniform distribution and low PEEQ values in members, as shown in Figure 20, the original, middle, and middle models were suggested for 6 TC-0 WR, 8 TC-0 WR, and 10 TC-0 WR, respectively. In addition, increasing the length of the columns may cause instability of the connection, resulting in a decreasing of the ultimate compressive resistance of the connection.

For a cost-effective and lighter FPLC, a weight reduction method was developed for the 6 TC-Original, 8 TC-Middle, and 10 TC-Middle models. It is acceptable if the ultimate load capacity decreases by less than 10%. Figure 24 presents the comparisons of the maximum acceptable weight reduction and 0% weight reduction models under compressive load with the length of the column 450 mm and the strength of the column Q355 and Table 4 lists their details. To conclude, the parametric study indicates that the 6 TC-Original-15 WR model is suitable for a low load-bearing capacity requirement. Meanwhile, the 8 TC-middle-15 WR is suitable for a high load-bearing capacity requirement.

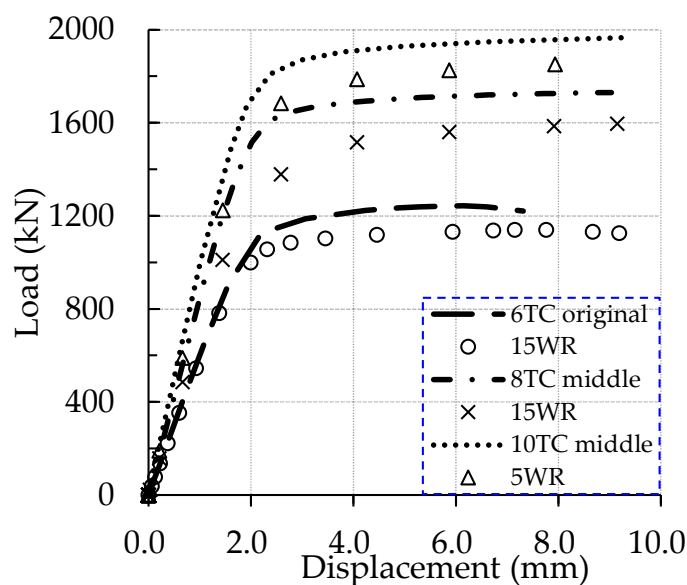


Figure 24. Axial compressive load behavior of different models.

Table 4. Comparisons of ultimate load-bearing capacity of FEM.

Series	Ultimate Load (kN)		<i>n</i> (%)
	0 WR	Maximum WR	
6 TC-Original	1242.9	1140.1 (15 WR)	8.27
8 TC-Middle	1733.1	1599.5 (15 WR)	7.71
10 TC-Middle	2124.2	1885.1 (5 WR)	11.27

Note: *n* denotes the reduction percentage of load bearing capacity between maximum WR model and 0 WR model.

7. Conclusions

This paper focuses on a new design for a fully prefabricated liftable connection (FPLC) with a standard corner fitting for modular steel construction. Five monotonic loading tests were performed to study the effect of bolt number and diameter on the axial load-bearing capacity of the FPLC. Three-dimensional FEM was developed to provide a better understanding of the stress and PEEQ distribution patterns of the connection and conduct the subsequent parameter research. From what has been discussed above, the following conclusions can be drawn.

1. The equivalent strain obtained from the test indicated that plastic strain occurred in columns earlier. The failure mode of the connection under axial compression is governed by local buckling of the column.
2. Full-scale experiment and nonlinear FEA on the innovative connection showed that ultimate load and yield load of the connection may apparently decrease with an increase of the areas of the bolt hole on the column wall. In other words, the axial load-bearing capacity of the FPLC may decrease as the diameter and number of the long stay bolts increase.
3. The location of the column on the corner fitting does not play a main role in the compressive strength of the FPLC. However, the location of the column affects the Von Mises stress and PEEQ distribution, and the original, middle, and middle column locations are suggested for columns with thicknesses of 6 mm, 8 mm, and 10 mm, respectively.
4. The compressive resistance of the connection is closely related to the thickness, length, and strength of the module column. Increasing the conditional yield strength of the columns increases the ultimate compressive load of the FPLC. Increasing the length of the column results in a decrease of the ultimate compressive-load capacity. The thick-

ness of the column occupies a main factor of the load capacity, and the failure mode may become inelastic global buckling when the thickness of the column increases.

5. The weight reduction (WR) of the corner fitting can be up to 15% in the 6 TC-Original and 8 TC-Middle models when the axial load-bearing capacity decreases by 8.27% and 7.71%, respectively. It is not suitable for the model with a column thickness of 10 mm to reduce the weight of the corner fitting because of an unacceptable decline in the magnitude of the ultimate load, even with a small amount of weight reduction.

Author Contributions: E.-F.D.: methodology, conceptualization, writing—review & editing, funding acquisition; J.-Y.L.: conceptualization, software, writing—original draft, writing—review & editing; Z.L.: supervision, investigation, funding acquisition; G.-C.Z.: investigation, writing—review & editing; S.-B.W.: resources, investigation, methodology; D.-B.C.: validation, visualization. All authors have read and agreed to the published version of the manuscript.

Funding: This research was supported by the Natural Science Foundation of China (Grant NO. 51908511), Shandong Provincial Natural Science Foundation (Grant NO. ZR2020QE247), the Key R&D Project (Major Scientific and Technological Innovation Project) of Shandong Province (2021CXGC011204), and the Key Research and Promotion Project (Scientific and Technological Project) of Henan Province, China (Grant NO. 212102310286).

Institutional Review Board Statement: Not applicable.

Informed Consent Statement: Not applicable.

Data Availability Statement: The data presented in this study are available on request from the authors.

Conflicts of Interest: The authors declare no conflict of interest.

References

1. Annan, C.D.; Youssef, M.A.; El-Naggar, M.H. Effect of directly welded stringer-to-beam connections on the analysis and design of modular steel building floors. *Adv. Struct. Eng.* **2009**, *12*, 373–383. [\[CrossRef\]](#)
2. Ye, Z.; Giriunas, K.; Sezen, H.; Wu, G.; Feng, D. State-of-the-art review and investigation of structural stability in multi-story modular buildings. *J. Build. Eng.* **2021**, *33*, 101844. [\[CrossRef\]](#)
3. Lacey, A.W.; Chen, W.; Hao, H.; Bi, K. Review of bolted inter-module connections in modular steel buildings. *J. Build. Eng.* **2019**, *23*, 207–219. [\[CrossRef\]](#)
4. Nadeem, G.; Safiee, N.A.; Bakar, N.A.; Karim, I.A.; Nasir, N.A.M. Connection design in modular steel construction: A review. *Structures* **2021**, *33*, 3239–3256. [\[CrossRef\]](#)
5. Ryan, E.S. *Prefab Architecture: A Guide to Modular Design and Construction*; John Wiley and Sons, Inc.: Hoboken, NJ, USA, 2010.
6. Corfar, D.; Tsavdaridis, K.D. A comprehensive review and classification of inter-module connections for hot-rolled steel modular building systems. *J. Build. Eng.* **2022**, *50*, 104006. [\[CrossRef\]](#)
7. Gatheeshgar, P.; Poologanathan, K.; Gunalan, S.; Shyha, I.; Sherlock, P.; Rajanayagam, H.; Nagaratnam, B. Development of affordable steel-framed modular buildings for emergency situations (COVID-19). *Structures* **2021**, *31*, 862–875. [\[CrossRef\]](#)
8. World's Tallest Prefab Skyscrapers Will Rise in Singapore—But They're Being Built in Malaysia. Available online: <https://edition.cnn.com/style/article/singapore-worlds-tallest-prefab-skyscraper-intl-hnk/index.html> (accessed on 14 April 2022).
9. Lawson, R.M.; Ogden, R.G. "Hybrid" light steel panel and modular systems. *Thin-Walled Struct.* **2008**, *46*, 720–730. [\[CrossRef\]](#)
10. Lawson, R.M.; Ogden, R.G.; Goodier, C. *Design in Modular Construction*; CRC Press: Boca Raton, FL, USA, 2014.
11. Kim, J.; Lee, J. A basic study on the application of modular construction. *J. Korean Hous. Assoc.* **2014**, *25*, 39–46. [\[CrossRef\]](#)
12. Park, H.K.; Ock, J.H. Unit modular in-fill construction method for high-rise buildings. *KSCE J. Civ. Eng.* **2015**, *20*, 1201–1210. [\[CrossRef\]](#)
13. Andrade, P.; Veljkovic, M.; Lundholm, J.; Heistermann, T. Innovative construction of student residences: Frameup concept. In Proceedings of the Nordic Steel Construction Conference: Tampere University of Technology, Department of Civil Engineering, Tampere, Finland, 23–25 September 2015; pp. 199–200.
14. Hou, H.; Yan, X.; Qu, B.; Lu, Y. Cyclic tests of steel tee energy absorbers for precast exterior wall panels in steel building frames. *Eng. Struct.* **2021**, *242*, 112561. [\[CrossRef\]](#)
15. Hou, H.; Zhang, S.; Qu, B.; Zhu, Y.; Liang, Y.; Liang, Y.; Li, K.; Fu, X. Low-rise steel moment-resisting frames with novel re-centering beam-to-column connections: Connection modelling and system performance evaluation. *J. Constr. Steel Res.* **2021**, *180*, 106578. [\[CrossRef\]](#)
16. Srisangeerthan, S.; Hashemi, M.; Rajeev, P.; Gad, E.; Fernando, S. Review of performance requirements for inter-module connections in multi-story modular buildings. *J. Build. Eng.* **2020**, *28*, 101087. [\[CrossRef\]](#)

17. Annan, C.D.; Youssef, M.A.; Naggar, M.H.E. Experimental evaluation of the seismic performance of modular steel-braced frames. *Eng. Struct.* **2009**, *31*, 1435–1446. [[CrossRef](#)]
18. Deng, E.; Zong, L.; Ding, Y.; Dai, X.; Lou, N.; Chen, Y. Monotonic and cyclic response of bolted connections with welded cover plate for modular steel construction. *Eng. Struct.* **2018**, *167*, 407–419. [[CrossRef](#)]
19. Chen, Z.; Liu, Y.; Zhong, X.; Liu, J. Rotational stiffness of inter-module connection in mid-rise modular steel buildings. *Eng. Struct.* **2019**, *196*, 109273. [[CrossRef](#)]
20. Dai, X.; Zong, L.; Ding, Y.; Li, Z. Experimental study on seismic behavior of a novel plug-in self-lock joint for modular steel construction. *Eng. Struct.* **2018**, *181*, 143–164. [[CrossRef](#)]
21. Sanches, R.; Mercan, O.; Roberts, B. Experimental investigations of vertical posttensioned connection for modular steel structures. *Eng. Struct.* **2018**, *175*, 776–789. [[CrossRef](#)]
22. Dhanapal, J.; Ghaednia, H.; Das, S.; Velocci, J. Structural performance of state-of-the-art VectorBloc modular connector under axial loads. *Eng. Struct.* **2019**, *183*, 496–509. [[CrossRef](#)]
23. Dhanapal, J.; Ghaednia, H.; Das, S.; Velocci, J. Behavior of thin-walled beam-column modular connection subject to bending load. *Thin-Walled Struct.* **2019**, *149*, 106536. [[CrossRef](#)]
24. Hou, H.; Wang, C.; Qu, B.; Liang, Y. Cyclic testing of bolted base connections for wide-flange columns. *Eng. Struct.* **2021**, *235*, 112024. [[CrossRef](#)]
25. Hou, H.; Sun, B.; Qu, B.; Wang, C.; Zhang, S.; Liang, Y. Testing of bolted base connections for wide-flange columns under combined axial compression and weak-axis lateral forces. *J. Constr. Steel Res.* **2021**, *179*, 106547. [[CrossRef](#)]
26. Chen, Z.; Wang, J.; Liu, J.; Khan, K. Seismic behavior and moment transfer capacity of an innovative self-locking inter-module connection for modular steel building. *Eng. Struct.* **2021**, *245*, 112978. [[CrossRef](#)]
27. Zhai, S.; Lyu, Y.; Cao, K.; Li, G.; Wang, W.; Chen, C. Experimental study on bolted-cover plate corner connections for column-supported modular steel buildings. *J. Constr. Steel Res.* **2022**, *189*, 107060. [[CrossRef](#)]
28. Deng, E.; Zong, L.; Ding, Y.; Zhang, Z.; Zhang, J.; Shi, F.; Cai, L.; Gao, S. Seismic performance of mid-to-high rise modular steel construction—A critical review. *Thin-Walled Struct.* **2020**, *155*, 106924. [[CrossRef](#)]
29. Styles, A.; Luo, F.; Bai, Y.; Murray-Parkes, J. Effects of joint rotational stiffness on structural responses of multi-story modular buildings. In Proceedings of the 2016 International Conference on Smart Infrastructure and Construction, ICSIC, Cambridge, UK, 27–29 June 2016; pp. 457–462. [[CrossRef](#)]
30. Sendanayake, S.V.; Thambiratnam, D.P.; Perera, N.J.; Chan, T.H.T.; Aghdamy, S. Enhancing the lateral performance of modular buildings through innovative inter-modular connections. *Structures* **2021**, *29*, 167–184. [[CrossRef](#)]
31. Lacey, A.W.; Chen, W.; Hao, H.; Bi, K.; Tallowin, F.J. Shear behaviour of post-tensioned inter-module connection for modular steel buildings. *J. Constr. Steel Res.* **2019**, *162*, 105707. [[CrossRef](#)]
32. Choi, K.; Lee, H.-C.; Kim, H. Influence of analytical models on the seismic response of modular structures. *J. Korea Inst. Struct. Maint. Insp.* **2016**, *20*, 74–85. [[CrossRef](#)]
33. CECS 334-2013; Technical Specification for Modular Freight Container Building. China Planning Press: Beijing, China, 2013. (In Chinese)
34. Zhang, J.; Tian, G.; Zhao, J.; Deng, E.; Wen, M.; Ye, L.; Guo, X.; Zhou, J.; Wang, S.Q.; Xing, X. Experimental Study on Seismic Performance of Connection for ATLS modular house. *J. Constr. Steel Res.* **2020**, *170*, 106118. [[CrossRef](#)]
35. GB/T 228.1-2010; Metallic Materials-Tensile Testing-Part 1: Method of Test at Room Temperature. China Quality Press, Standards Press of China: Beijing, China, 2010. (In Chinese)
36. EN 1993-1-1; Design of Steel Structures-Part 1-1: General Rules and Rules for Buildings. European Standard: London, UK, 2005.
37. JJF 1296.2-2011; Program of Pattern Evaluation of Static Uniaxial Testing Machines-Part 2: Electro-Hydraulic Servo Universal Testing Machines. General Administration of Quality Supervision, Inspection and Quarantine of the People's Republic of China: Beijing China, 2011. (In Chinese)
38. ABAQUS. *User Manual Version 6.13*; DS SIMULIA Corp: Providence, RI, USA, 2013.
39. Fleischman, R.B.; Li, X.; Pan, Y.; Sumer, A. Cast Modular Panel Zone Node for Steel Special Moment Frames. I: Analytical Development. *J. Struct. Eng. ASCE* **2007**, *133*, 1393–1403. [[CrossRef](#)]
40. Lima, J.M.; Bezerra, L.M.; Bonilla, J.; Barbosa, W.C.S. Study of the behavior and resistance of right-angle truss shear connector for composite steel concrete beams. *Eng. Struct.* **2022**, *253*, 113778. [[CrossRef](#)]
41. Ellobody, E.; Young, B. Behavior of cold-formed steel plain angle columns. *J. Struct. Eng.* **2005**, *131*, 457–466. [[CrossRef](#)]
42. Shi, G.; Zhou, W.; Bai, Y.; Lin, C. Local buckling of 460 MPa high strength steel welded section stub columns under axial compression. *J. Constr. Steel Res.* **2014**, *100*, 60–70. [[CrossRef](#)]